Monthly Notices of the ROYAL ASTRONOMICAL SOCIETY

MNRAS **540,** 3311–3329 (2025) https://doi.org/10.1093/mnras/staf899
Advance Access publication 2025 June 06

GA-NIFS: witnessing the complex assembly of a star-forming system at $z = 5.7$

Gareth C. Jones [1,2,3★] Andrew J. Bunker,[1] Kseniia Telikova [4] Santiago Arribas,[5] Stefano Carniani [6] Stephane Charlot [7] Francesco D'Eugenio [2,3] Roberto Maiolino [2,3,8] Michele Perna,[5] Bruno Rodríguez Del Pino,[5] Hannah Übler [2,3,9] Chris Willott,[10] Manuel Aravena,[4] Torsten Böker [11] Giovanni Cresci,[12] Mirko Curti,[13] Jorge González-López,[14,15] Rodrigo Herrera-Camus,[16] Isabella Lamperti [5,12,17] Eleonora Parlanti,[6] Pablo G. Pérez-González[5] and Vicente Villanueva[16]

Affiliations are listed at the end of the paper

Accepted 2025 May 27. Received 2025 March 26; in original form 2024 May 21

ABSTRACT

We present observations of the $z \sim 5.7$ Lyman-break galaxy HZ10 with the *JWST*/NIRSpec integral field unit in high and low spectral resolution (G395H, spectral resolving power $R \sim 2700$ and PRISM, $R \sim 100$, respectively), as part of the GA-NIFS programme. By spatially resolving the source (spatial resolution $\sim 0.15''$ or ~ 0.9 kpc), we find three spatially and spectrally distinct regions of line emission along with one region of strong continuum emission, all within a projected distance of < 10 kpc. The R2700 data features strong detections in Hβ, [O III] $\lambda\lambda$4959,5007, [N II] $\lambda\lambda$6548,6584, Hα, and [S II] $\lambda\lambda$6716,6731. The R100 data additionally contain a strong detection of the Ly α break, rest-frame UV and optical continuum, and [O II] $\lambda\lambda$3726,3729. None of the detected lines present strong evidence for active galactic nucleus excitation from line diagnostic diagrams, and no high-ionization lines are detected. Using the detected lines, we constrain the electron density $\left(\log_{10}\left(n_e/\mathrm{cm}^{-3}\right) \sim 3\right)$ and metallicity ($\sim 0.5 - 0.7$ solar) in each component. Spaxel-by-spaxel fits reveal a strong east-west velocity gradient and significant line asymmetries (possibly indicating tidal features or outflows). The western component features a very red UV slope ($\beta_{\mathrm{UV}} \sim -0.9$) and significant H α emission, suggesting an evolved population and active star formation. A comparison to high-resolution (~ 0.3 arcsec or ~ 1.8 kpc) [C II] 158 μm imaging obtained with the Atacama Large Millimetre/submillimetre Array (ALMA) reveals areas of dust obscuration. Altogether, these data suggest that HZ10 represents an ongoing merger, with a complex distribution of stars, gas, and dust < 1 Gyr after the big bang

Key words: galaxies: high-redshift – galaxies: interactions – galaxies: ISM – galaxies: kinematics and dynamics.

1 INTRODUCTION

Studies of local galaxies have shown that the majority of them are relaxed disks with spiral arms (e.g. Delgado-Serrano et al. 2010). But when the Universe was much younger ($\lesssim 1.5$ Gyr after the big bang, $z > 4$), this was not the case. In the early Universe, observational studies have found that the fraction of galaxies with spiral features decreases with increasing redshift (Kuhn et al. 2024), while the major merger fraction increases with redshift (e.g. Rodrigues et al. 2017; Duncan et al. 2019; Ferreira et al. 2020). A survey of $z \sim 4$–6 galaxies with the Atacama Large Millimetre/submillimetre Array (ALMA) revealed a small fraction of rotating discs, with a high number of mergers (e.g. Le Fèvre et al. 2020; Jones et al. 2021; Romano et al. 2021; The ALMA Large Program to Investigate [C II] at Early Times; ALPINE). This agrees with the results of cosmological zoom-in simulations of high-redshift galaxies, which show that the evolution of these sources is heavily influenced by frequent major and minor mergers (e.g. Pallottini et al. 2017; Kohandel et al. 2019; Kretschmer, Dekel & Teyssier 2022).

Since the secure identification of merging activity requires resolved observations of galaxy kinematics (e.g. Simons et al. 2019), much progress has been made through ALMA observations of the strong far-infrared (FIR) emission line [C II] 158 μm (hereafter [C II]). In general, [C II] observations of $z > 4$ galaxies tend to show multiple star-forming clumps or extensions (e.g. Carilli et al. 2013; Bischetti et al. 2018; Carniani et al. 2018; Le Fèvre et al. 2020; Nguyen et al. 2020). Some high spatial resolution ($\sim$ 1–3 kpc) [C II] observations of these galaxies reveal the presence of ordered rotation (e.g. Neeleman et al. 2020; Rizzo et al. 2020; Fraternali et al. 2021; Lelli et al. 2021; Tsukui & Iguchi 2021; Herrera-Camus et al. 2022; Posses et al. 2023; Roman-Oliveira, Fraternali & Rizzo 2023), but often with nearby companions or departures from regular rotation that could indicate the influence of a nearby merging companion galaxy.

These ALMA observations are powerful tools for determining the morpho-kinematics of the cold interstellar medium (ISM) in these galaxies, and may be used to estimate dust properties (from the FIR

★ E-mail: gj283@cam.ac.uk

spectral energy distribution; SED), dynamical mass, ISM properties (e.g. temperature, density, strength of the radiation field; Novak et al. 2019; Harikane et al. 2020; Hashimoto et al. 2023a) and either the molecular gas mass (e.g. Zanella et al. 2018; Vizgan et al. 2022a) or star formation rate (SFR; e.g. De Looze et al. 2014; Schaerer et al. 2020). A complementary view of the ISM and galaxy properties in the context of their morpho-kinematics (including the existence of feedback from the nuclear region; e.g. Perna et al. 2020; Fluetsch et al. 2021; Cresci et al. 2023) is enabled through observations of ionized lines in the rest-optical. With the advent of the *JWST* and the integral field unit (IFU; Böker et al. 2022) on the Near Infrared Spectrograph (NIRSpec; Jakobsen et al. 2022), we may now conduct spatially resolved observations of high-redshift galaxies in rest-UV and rest-optical continuum emission and emission lines, shedding light on stellar populations and the ISM.

The NIRSpec IFU has been used to characterize the morpho-kinematics and ISM conditions for multiple systems of $z > 4$ galaxies (e.g. Hashimoto et al. 2023b; Loiacono et al. 2024; Venturi et al. 2024), with a large portion of the observations originating from the Galaxy Assembly with NIRSpec Integral Field Spectroscopy (GA-NIFS[1]) Guaranteed Time Observations (GTO) programme (PIs: R. Maiolino & S. Arribas; e.g. Marshall et al. 2023; Übler et al. 2023; Arribas et al. 2024; Ji et al. 2024; Parlanti et al. 2024; Jones et al. 2024a; Übler et al. 2024a, b). This programme contains observations of 55 diverse galaxies (e.g. quasar host galaxies, star-forming galaxies, rotators, mergers) between $z \sim 2$–11 with the NIRSpec IFU (see also Perna et al. 2023; D'Eugenio et al. 2024; Pérez-González et al. 2024; Rodríguez Del Pino et al. 2024; Perna et al. 2025). In this work, we analyse data from GA-NIFS observations of the galaxy HZ10 at $z \sim 5.7$.

HZ10 was originally detected as a Lyman break galaxy (LBG) in the 2 square degree Cosmic Evolution Survey (COSMOS; Scoville et al. 2007) field. Photometric observations with Subaru/Suprime-Cam revealed evidence for significant Lyα emission at $z \sim 5.7$ (observed-frame equivalent width of 75 ± 22 Å; source 66 of Murayama et al. 2007). Follow-up observations with the Deep Extragalactic Imaging Multi-Object Spectrograph (DEIMOS) on the W. M. Keck-II Observatory revealed that this source is a UV-luminous ($M_{\rm UV} = -22.56 \pm 0.15$) Ly$\alpha$ emitter at $z_{\rm sys} = 5.659$, with a red UV slope ($\beta_{\rm UV} < -0.6$) and a large stellar mass ($\log_{10}(M_*/{\rm M}_\odot) = 10.39 \pm 0.17$; Capak et al. 2015). It was selected as one of the first high-redshift objects to be observed in [C II] emission with ALMA (project 2012.1.00523.S, PI: P. Capak).

In the sample of 10 $z \sim 5.1$–5.7 LBGs in Capak et al. (2015), HZ10 was the brightest ($S_{158\mu{\rm m}} = 1.261 \pm 0.044$ mJy) and largest [beam-deconvolved full width at half-maximum (FWHM) of $(1.16 \pm 0.11)'' \times (0.59 \pm 0.03)''$ at $83.2 \pm 3.1°$] FIR continuum source. Based on this detection and assuming a modified blackbody model, Capak et al. estimate an infrared luminosity $\log_{10}(L_{\rm IR}/L_\odot) = 11.94 \pm 0.08$ and $SFR_{\rm IR} = 169^{+32}_{-27}$ ${\rm M}_\odot$ yr^{-1}. Both the [C II] and FIR continuum emission of HZ10 feature an east-west elongation, where the eastern end overlaps with UV emission (Subaru z' band).

Further analysis of the [C II] data by Pavesi et al. (2016) returned a precise $z_{\rm [C\,II]} = 5.6543 \pm 0.0003$, $\log_{10}(L_{\rm [C\,II]}/L_\odot) = 9.60 \pm 0.03$, and the detection of a velocity gradient (FWHM~ 630 km s^{-1}). While [N II] 205 μm was significantly detected ($> 3\sigma$), it featured a smaller FWHM, was redshifted, and spatially extended to the west. Based on the observed properties, Pavesi et al. suggest that HZ10 may represent an ongoing major merger. Kinematic modelling of the [C II] data cube (Pavesi et al. 2019) resulted in a dynamical mass estimate of $\log_{10}(M_{\rm dyn}/{\rm M}_\odot) = 10.79 \pm 0.05$, in agreement with other analyses (Capak et al. 2015; Jones et al. 2017).

This source has also been detected in CO(2–1) emission (Pavesi et al. 2019), where an assumed conversion factor of $\alpha_{\rm CO} = 4.5\,{\rm M}_\odot\,{\rm K}^{-1}\,{\rm km}^{-1}\,{\rm s\,pc}^{-2}$ yielded a molecular gas mass of $\log_{10}(M_{\rm gas}/{\rm M}_\odot) = 11.1 \pm 0.1$. Follow-up observations of CO(5–4) and CO(6–5) (Vieira et al. 2022) did not recover significant emission. A detection of C III] λ1909 enabled Markov et al. (2022) to estimate the gas-phase metallicity[2] of HZ10 ($Z = 0.60^{+0.32}_{-0.52} Z_\odot$).

A massive starburst galaxy (CRLE, $z = 5.667$) nearby to HZ10 ($13'' \sim 77$ kpc in projected distance; $\Delta v \sim 580$ km s^{-1}) was serendipitously detected through [C II], [N II]205 μm, and CO(2-1) observations (Pavesi et al. 2018). A further search of the COSMOS2015 photometric redshift catalogue (Laigle et al. 2016) revealed the presence of a galaxy overdensity (eight galaxies within $3'$ of CRLE).

Altogether, these previous findings present a complex picture of HZ10. It is gas-rich, dynamically massive, and FIR bright. But its asymmetric velocity field and frequent spatial shift between tracers (e.g. [C II] and [N II]) argue against a single source. One possible route towards determining the nature of this galaxy is to examine the rest-frame optical properties of this object on a resolved scale, which was not previously possible.

In this work, we present new *JWST*/NIRSpec IFU observations of HZ10 to further investigate this well-studied, but still mysterious system. The details of our observations and calibration procedure are given in Section 2. These data are analysed in Section 3, and we discuss the results in Section 4. We conclude in Section 5. We assume a standard concordance cosmology (Ω_Λ, Ω_m, h) = (0.7,0.3,0.7) throughout. At the approximate redshift of this source ($z = 5.6543$, based on the [C II] data of Capak et al. 2015 and Pavesi et al. 2016), 1 arcsec corresponds to 5.90 projected kpc. Emission lines are named based on their air wavelength, while we use their vacuum wavelengths for analysis (e.g. $\lambda_{\rm rest,[O\,III]\lambda5007} = 5008.24$ Å).

Table 1. *JWST* NIRSpec/IFU observation properties.

Grating/filter	G395H/290LP	PRISM/CLEAR
Readout pattern	NRSIRS2	NRSIRS2RAPID
Groups/int	31	33
Ints/exp	1	1
Exposures	8	8
Total time (ks)	18.2	4.0

2 OBSERVATIONS AND CALIBRATION

The data analysed here originated from GA-NIFS observations as part of project 1217 (PI: N. Luetzgendorf; details in Table 1). An eight-point 'MEDIUM' dither pattern was used, with a starting point of '1'. Data were taken at both low (PRISM/CLEAR; spectral resolving power $R \sim 100$; 0.60–5.30 μm, hereafter R100) and high spectral resolution (G395H/F290LP; $R \sim 2700$; $2.87 - 5.14$ μm, hereafter R2700). The data were calibrated with the STScI pipeline (v11.1, CRDS 1149), with custom outlier rejection (D'Eugenio et al. 2024), custom masks for cosmic ray strikes ('snowballs') or open MSA shutters, 1/f noise corrections for count-rate maps, and drizzle weighting to create data cubes with spatial pixels (spaxels) of width

[1] https://ga-nifs.github.io/

[2] This metallicity was derived by combining the observed C III] λ1909 and [C II] fluxes with the model of Vallini et al. (2020).

0.05″ (see Perna et al. 2025 for full details of reduction). Previous works targeting bright targets with the *JWST*/NIRSpec IFU revealed sinusoidal 'wiggle' patterns in spectra extracted from single spaxels (e.g. Perna et al. 2023; Decarli et al. 2024; Ulivi et al. 2025). These patterns, caused by under-sampling of the point spread function (PSF), do not appear in our data at high significance (i.e. $> 1\sigma$), so we do not apply the correction of Perna et al. (2023).

To verify the astrometry of our data, we first downloaded *HST*/WFC3 images from the Mikulski Archive for Space Telescopes (MAST[3]) archive (F125W, F160W, F105W). These images have been aligned to the *Gaia* DR3 reference frame (Gaia Collaboration 2016, 2021), and are well-suited for astrometric comparison. Comparison images were created by convolving the R100 data cube with each *HST*/WFC3 filter bandpass function. No significant offset (i.e. > 0.1 arcsec) between the *Hubble Space Telescope* (*HST*) and *JWST* images was found, so no astrometric correction was performed. We have also confirmed that the R100 and R2700 cubes are aligned to the same frame (see Appendix A).

No background exposures were included in these observations, so we manually performed a background subtraction for each cube (R100 and R2700) following a procedure similar to that utilized by other NIRSpec IFU studies (e.g. Ji et al. 2025; Scholtz et al. 2025a). First, we mask all data in the cube that falls outside the IFU footprint and apply sigma clipping (2.5σ) to exclude emission. Using the PHOTUTILS task *Background2D* with a 14×14 spaxel (0.7 arcsec $\times$ 0.7 arcsec) square window and a 5×5 spaxel median filter, we determine approximate background maps of each spectral channel in the data cube. These background maps are visually inspected to verify that they do not contain emission (i.e. line or continuum), and are then subtracted from the observed data cube.

3 ANALYSIS

3.1 Overview of continuum and line emission

An initial investigation of the IFU data cubes revealed that HZ10 is composed of multiple regions of strong emission. To illustrate this, we compare the $\lambda_{\rm obs} = 4\,\mu$m continuum (stellar emission at $\lambda_{\rm rest} \sim 6000$ Å) and [O III] λ5007 emission from our R2700 data in Fig. 1 (see Section 3.3.1 for details of the creation of this map). It is clear that the line emission is concentrated in three components (here called HZ10-E, HZ10-C, and HZ10-W), while the rest-optical continuum is located at the position of HZ10-W and to the north of HZ10-E and HZ10-C. We define four apertures for further study: three circular apertures (radius 0.125″) centred on the line peaks of each component (white circles in Fig. 1) that contain most of the line emission, and one larger ellipse that contains all significant emission (large dashed white ellipse in Fig. 1).

Our ability to detect individual regions is partly due to the narrow PSF of our data (FWHM < 0.2 arcsec) compared to previous ALMA observations (FWHM > 0.6 arcsec; Capak et al. 2015). HZ10-E and HZ10-C are only separated by a projected distance of ~ 0.27 arcsec (~ 1.6 kpc), so previous observations lacked the resolution to separate them (although see novel high-resolution ALMA [C II] observations of HZ10; Telikova et al. 2024; Villanueva et al. 2024).

We characterize the emission in this field using two methods. First, we analyse emission from the line peaks (see white circles in Fig. 1; Section 3.2). Next, in Section 3.3 we take advantage of our high spatial resolution by performing spaxel-by-spaxel fits to each data cube. In addition to these analyses, we examine the full field by extracting an integrated spectrum from the R100 data cube using the large dashed white ellipsoidal aperture of Fig. 1 (Appendix B).[4]

3.2 Component analysis

We begin by extracting integrated spectra from the R100 and R2700 cubes using the three emission line-focused apertures and fitting the line and continuum emission. We include H β, [O III] λ4959, [O III] λ5007, [N II] λ6548, H α, [N II] λ6584, [S II] λ6716, and [S II] λ6731 in the R2700 fit, while the wider spectral coverage of the R100 data ($\sim 0.6 - 5.2\,\mu$m) allows us to also fit [O II] $\lambda\lambda$3726,3729. A corrected error spectrum is derived by rescaling the pipeline-output error array to match the standard deviation of sigma-clipped data (e.g. Jones et al. 2024a; Übler et al. 2024a). For R100, we derive the scaling factor using data in a spectrally flat region ($\sim 4\,\mu$m).

We adopt the standard assumptions of [N II] λ6584/[N II] λ6548 $= 2.94$ (e.g. Dojčinović, Kovačević-Dojčinović & Popović 2023) and [O III] λ5007/[O III] λ4959 $= 2.98$ (e.g. Dimitrijević et al. 2007) for each fit. The ratio [S II] λ6716/[S II] λ6731 is a strong tracer of electron density, and is restricted to a range of ~ 0.55–1.45, assuming $T_e = 10^4$ K (e.g. Le Tiran et al. 2011; Della Bruna et al. 2020). Due to the low spectral resolution, we model [O II] $\lambda\lambda$3726,3729 as a single Gaussian.

For the R2700 spectra, we allow each line to contain a narrow and broad model component at different redshifts ($z_{\rm N}$ for all narrower components, and $z_{\rm B}$ for all broader components). This represents a two-zone model, where the narrow emission originates from core galaxies and the broad component may originate from nearby tidal features or outflows. This assumption is inspected further in Section 3.3.1 and Appendix C.

To allow for the suppression of [O III] $\lambda\lambda$4959,5007 and other forbidden lines in high-density environments (see Section 4.1.1), we separate the FWHM values of the Balmer lines (H α and H β) from the other lines. That is, we fit four FWHM values (in km s^{-1}) for each extracted spectrum: the narrow and broad FWHMs for the Balmer lines, and the narrow and broad FWHMs for the other lines. We account for the effect of the spectral resolving power on each linewidth when calculating each FWHM in the R2700 spectrum by adding the modelled intrinsic linewidth and instrumental line spread function (LSF[5]) in quadrature.

The line widths of the R100 fits are set using the fiducial LSF (i.e. each line is assumed to be unresolved in velocity space). Previous investigations using the micro-shutter assembly (MSA) on NIRSpec have found that the true LSF is narrower than the fiducial profile (e.g. de Graaff et al. 2024; Jones et al. 2024a). This is due to the fact that the fiducial spectral resolving power curve was derived assuming a uniformly lit MSA slit (width 0.2 arcsec), while many targets did not fill the slit. However, the IFU constructs data cubes using an image slicer with a narrower width (0.1″), so the fiducial LSF should be appropriate for our analysis. Regardless, the LSF-deconvolved width of the R100 lines is not used in this work. Future works will investigate the LSF of the IFU in more detail.

[3] https://mast.stsci.edu/portal/Mashup/Clients/Mast/Portal.html

[4] Due to the complex morphokinematics of the field (e.g. see Section 3.3.1), we do not consider the full-field spectrum from the R2700 data cube.

[5] As recorded in the *JWST* documentation; https://jwst-docs.stsci.edu/jwst-near-infrared-spectrograph/nirspec-instrumentation/nirspec-dispersers-and-filters

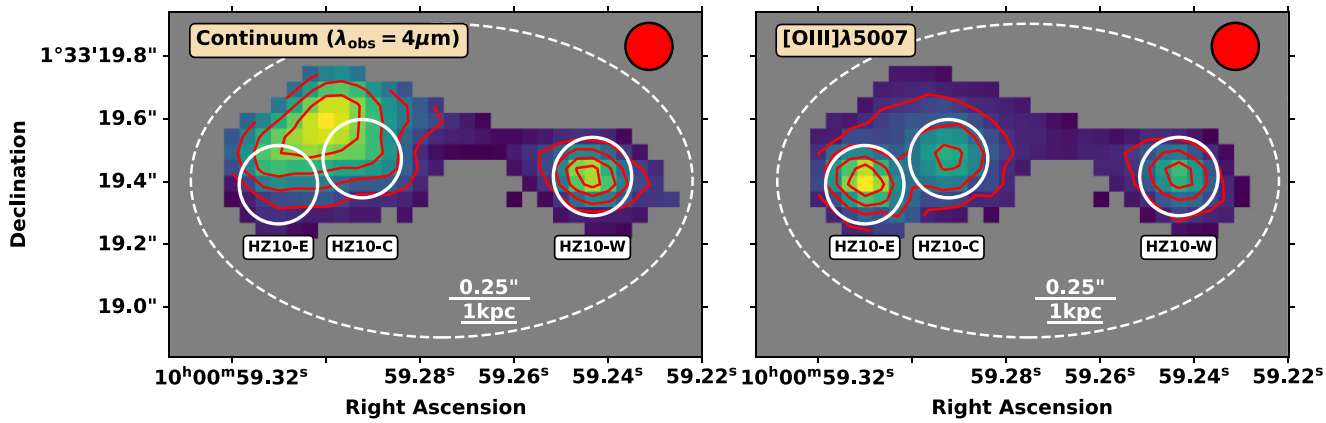

Figure 1. Demonstration of how emission in the HZ10 field is distributed. The colour and red contours show the $\lambda_{obs} = 4$ μm continuum level (left panel) and [O III] λ5007 emission (right panel) as derived from spaxel-by-spaxel fits to the R2700 data cube (see Section 3.3.1). Contours are shown at [20, 40, 60, 80] per cent of the maximum value of each map. The line emission is concentrated in three regions, which we denote as HZ10-E, HZ10-C, and HZ10-W (increasing in redshift and moving from east to west). The apertures we use to extract spectra of each component ($r = 0.125''$; Section 3.2) are shown as labelled white circles. A large white dashed ellipse marks the extraction aperture for the analysis of Appendix B. The fiducial PSF of the data (FWHM = 0.15 arcsec) is shown by a red ellipse to the upper right. Scales of 0.25″ and 1 kpc (at a systemic redshift of $z = 5.6543$) are shown by white lines. North is up and east is to the left.

The continuum of the R2700 spectrum is taken into account by including a single power law in the model with slope α_{opt}^{R2700}. For the R100 spectrum, the Ly α break was modelled using a Heaviside function. To allow for a discontinuity around the Balmer break, we fit the continuum redwards and bluewards of a Balmer series line (Hη, $\lambda_{rest} = 3837$ Å) with separate power law models (slopes α_{opt}^{R100} and β_{UV}^{R100}). Previous studies have found that the continuum redwards of the Lyα break may deviate from the single power law seen at rest-UV wavelengths (e.g. Cameron et al. 2024; Jones et al. 2024b). This effect is accounted for by fitting the continuum bluewards of a pivot wavelength ($\lambda_{rest} = 0.15$ μm) with a separate power law component (slope $\beta_{Ly\alpha}^{R100}$), such that the model is continuous at $\lambda_{rest} = 0.15$ μm. Due to the low spectral resolution of these data, we convolve the continuum model with a wavelength-dependent Gaussian representing the LSF (e.g. Heintz et al. 2024; Napolitano et al. 2024; Umeda et al. 2024; Jones et al. 2024a).

Each spectrum is fit with LMFIT (Newville et al. 2014) in 'least_squares' mode, using inverse variance weighting. The resulting best-fitting models are shown in Fig. 2 for R2700 data and Fig. 3 for R100 data. The best-fitting parameters are presented in Table 2.

3.2.1 *Spectral fit results*

The spectra of all three components are well-fit with our models, resulting in low residuals and estimates of redshift, UV magnitude, spectral slopes, line-widths, and line fluxes.

We are able to measure z_{sys} from the R100 spectra, as well as the redshifts of the narrow (z_N) and broad contributions (z_B) in the R2700 spectra. For all components, the R100-based redshift is $> 3\sigma$ higher than the average of the narrow and broad R2700-based redshifts ($z_{R100} - z_{R2700} = 0.006$–$0.009$). To explain this, we note that recent NIRSpec studies using the MSA (e.g. D'Eugenio et al. 2025) have found a spectral offset between R100 and R1000 data due to NIRSpec wavelength calibration issues ($z_{R100} - z_{R1000} \sim 0.004$–$0.005$; Bunker et al. 2024; D'Eugenio et al. 2025; Jones et al. 2025). Since this affects all NIRSpec observations, IFU data may be affected as well, as confirmed by the NIRSpec/IFU analysis of Pérez-González et al. (2024). These authors measured a redshift difference between the R100 and R2700 data for Hyde ($z_{R100} - z_{R2700} = 0.0075$), which is larger than the R100-R1000 redshift offset measured for NIRSpec/MSA observations but is comparable to our measured redshift offsets for HZ10. Because the R2700 redshift is in better agreement with the ALMA-based redshift, we only use redshifts based on the R2700 data in this work.

Taking the [C II] redshift of Pavesi et al. (2016) as the systemic redshift, we see that all three components feature blueshifted narrow emission with broad emission that is relatively redshifted (see Table 2). The line emission from the broad component of HZ10-W is much stronger than that of the narrow component, possibly indicating outflows or tidal interactions (see Section 4.3.1). The total velocity difference between the narrow components of HZ10-E and HZ10-W is large ($\sim 660\,km\,s^{-1}$), but the difference between the other component pairs is $< 500\,km\,s^{-1}$.

None of the R100 spectra show evidence for significant Ly α emission. Since the previously reported detection of Ly α in HZ10 (Murayama et al. 2007) used a larger aperture, we also search for Ly α using the dashed ellipse in Fig. 1 (see analysis of Appendix B). Even with a broader aperture, we do not detect Ly α. However, our 3σ upper limit on the rest-frame equivalent width of Ly α is in agreement with that of Murayama et al. (2007), suggesting that higher sensitivity observations are required.

The best-fitting rest-optical slopes (α_{opt}) of the R100 and R2700 data are in agreement ($< 3\sigma$ discrepant). The best-fitting power-law slopes bluewards of $\lambda_{rest} = 1500$ Å ($\beta_{Ly\alpha}^{100}$) are all more red than β_{UV}^{100}, which may be caused by a number of physical conditions (e.g. nebular or two-photon continuum, AGN activity, damped Ly α absorbers; Cameron et al. 2024; Tacchella et al. 2025; Witstok et al. 2025). Of the three components, HZ10-C is the most UV-bright ($M_{UV} = -20.67 \pm 0.01$) and features the bluest continuum slope ($\beta_{UV}^{100} = -1.99 \pm 0.01$). On the other hand, HZ10-W is the most UV-faint ($M_{UV} = -19.4 \pm 0.04$) and features the reddest continuum slope ($\beta_{UV}^{100} = -1.04 \pm 0.03$), and HZ10-E is intermediate in both measures. This is discussed further in Section 4.3.

3.2.2 *Line ratio analysis*

Using the line fluxes from the spectral analysis detailed in the previous subsection, we next explore the position of these com-

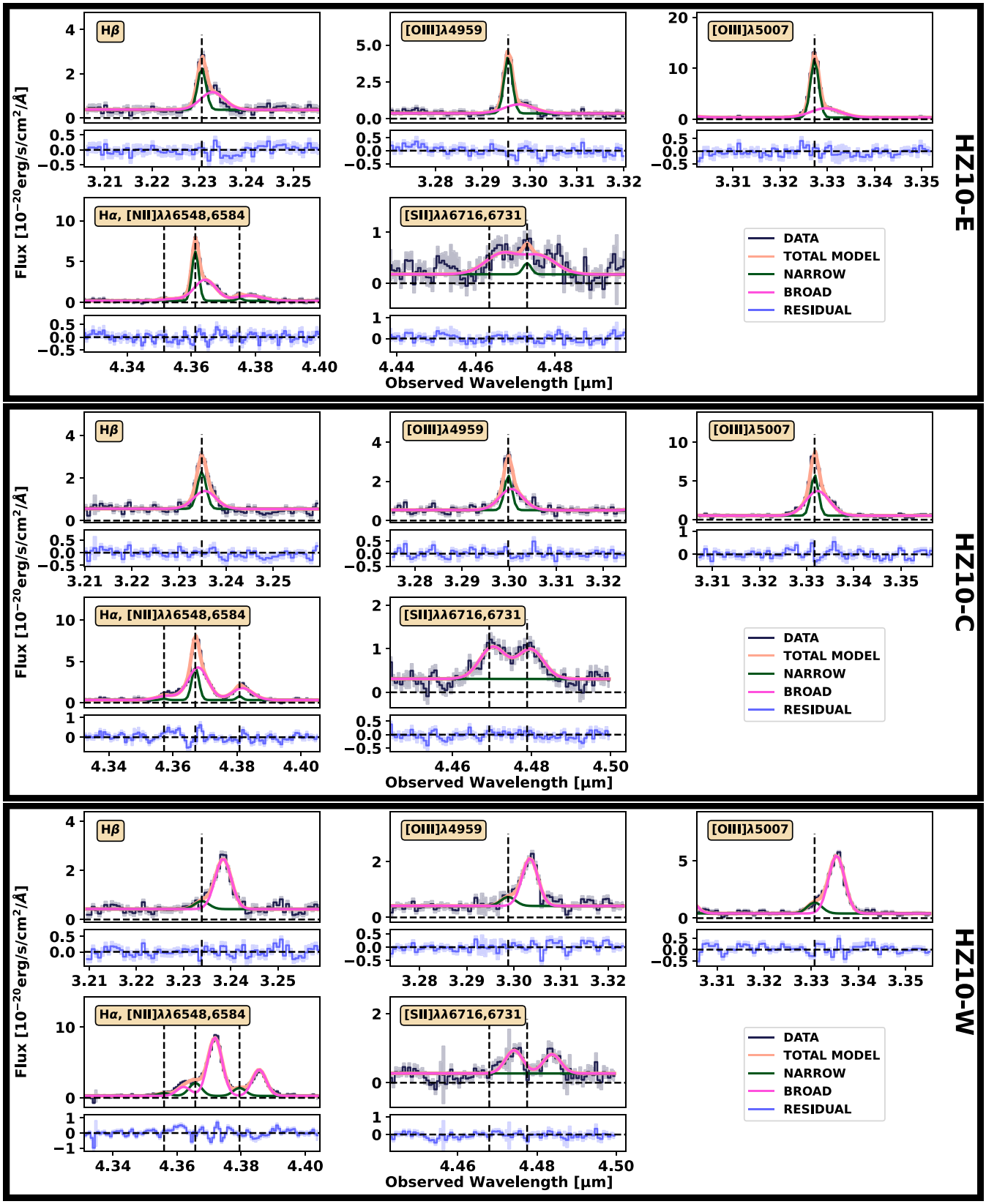

Figure 2. Spectra extracted from R2700 data cube using the circular apertures of Fig. 1 for each component (black lines). The best-fitting model is shown (tan lines), as well as the best-fitting narrow (green lines) and broad contributions (pink lines). Model residuals are shown in the lower portion of each panel (blue lines). The best-fitting centroid wavelengths of the narrow components of each line are shown by dashed vertical lines. We only show the wavelength range around studied emission lines. Uncertainties (1σ) for the extracted spectrum and residuals are shown by shaded regions.

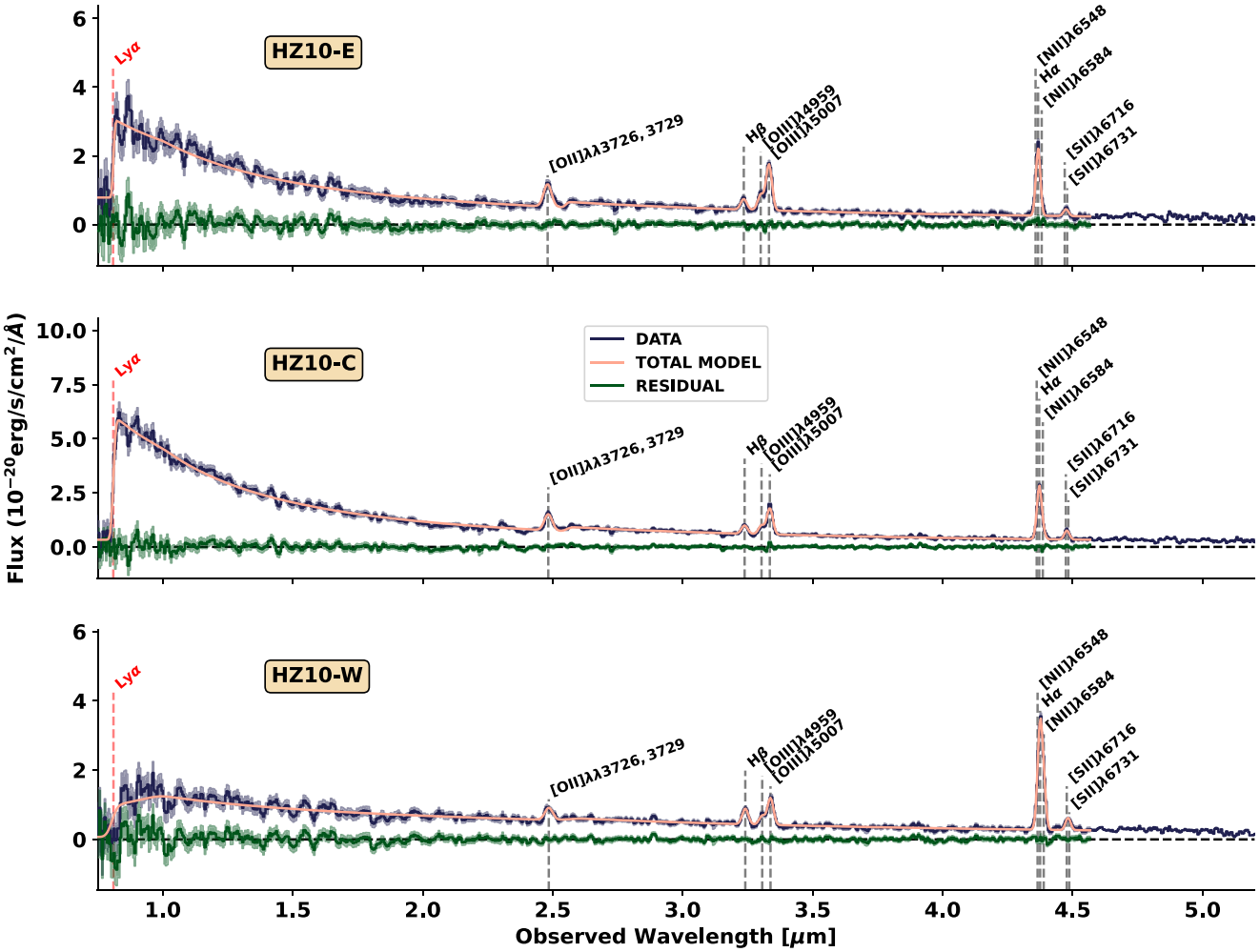

Figure 3. Spectra extracted from R100 data cube using the circular apertures of Fig. 1 for each component (black lines). The best-fitting models are shown by tan lines, as well as the residuals (green lines). The wavelengths of each line (using the best-fitting z_{sys}) are shown by dashed vertical lines. The expected wavelength of Ly α (which is not detected) is marked with a dashed red line. Uncertainties (1σ) for the extracted spectrum and residuals are shown by shaded regions.

ponents on line ratio diagrams (see Table 3 for definitions of ratios used in this work). These include the [N II]-BPT ($\log_{10}$R3 versus $\log_{10}$N2; Baldwin, Phillips & Terlevich 1981) and [S II]-VO87 ($\log_{10}$R3 versus $\log_{10}$S2; Veilleux & Osterbrock 1987) diagrams. Historically, these plots have been used to determine if galaxies are primarily powered by star formation (low N2, R3, and S2), AGN (high N2, R3, and S2), or a composite of the two (intermediate N2 and R3; e.g. Ibar et al. 2015; Mazzilli Ciraulo et al. 2021; Richings, Faucher-Giguère & Stern 2021). While the standard demarcation lines (Kewley et al. 2001; Kauffmann et al. 2003b) are suitable for high-metallicity, massive systems, they were derived for low-redshift galaxies. Some models and observations suggest that these criteria are not suitable for low-metallicity sources at high-redshift ($z > 4$; e.g. Feltre, Charlot & Gutkin 2016; Nakajima & Maiolino 2022; Übler et al. 2023; Dors et al. 2024; Maiolino et al. 2024b). Indeed, the location of galaxies on these diagrams is affected by a number of parameters (e.g. Z, presence of shocks, ionization parameter, hydrogen density; Allen et al. 2008; Feltre et al. 2016; Sugahara et al. 2021), so additional diagnostics are required for concrete conclusions. In this work, we utilize the demarcation lines of Scholtz et al. (2025b), which were derived from *JWST*/NIRSpec observations to separate extreme AGN (above each line) from all other sources at high redshift (including both weaker AGN and SFGs; below each line).

The resulting diagnostic plots are presented in Fig. 4. Due to the construction of our models, we may examine the flux ratios of the best-fitting narrow (blue outlined symbols), broad (red outlined symbols), and total model (black outlined symbols) for each component. Using the best-fitting line fluxes from fits of the R2700 data, we find that the components of HZ10 feature similar line ratios to other observed $z = 5.5 - 7.0$ galaxies (Cameron et al. 2023; Decarli et al. 2024; Jones et al. 2024a). All components fall underneath the Scholtz et al. (2025b) line for the [N II]-BPT diagram (except for the narrow component of HZ10-W), but both of the total best-fitting models for HZ10-E and HZ10-W lie on the demarcation line for the [S II]-VO87 relation. The broad components and upper limits on the narrow components of HZ10-C and HZ10-E lie above the [S II]-VO87 relation demarcation line, adding slight evidence for the presence of an AGN. Because none of the components lie far above the demarcation lines in both plots, there is no strong evidence for the presence of an AGN, although AGN contribution cannot be ruled out (see Section 4.1).

Table 2. Best-fitting line properties for HZ10, derived through separate fits to spectra extracted from $r = 0.125''$ circular apertures centred on each component (see Figs 2 and 3). Results are listed for the R100 (first set of rows) and R2700 spectra (second set of rows) using multi-Gaussian and continuum models. FWHM values are given in km s^{-1}, while integrated fluxes are in 10^{-20}erg s^{-1} cm^{-2}. For definitions of spectral slopes, see Section 3.2. The R100-based $z_{\rm sys}$ value is not used in this analysis. Velocity offsets are given with respect to $z_{\rm [C\,II]} = 5.6543$ (Pavesi et al. 2016). We present best-fitting fluxes for each line for the R100 and R2700 data. For the R2700 data, we additionally list the best-fitting narrow and broad components of the best-fitting models. Output uncertainties are given as 1σ, and upper limits are given at 3σ.

	HZ10-E	HZ10-C	HZ10-W
$z_{\rm sys}$	5.6528 ± 0.0006	5.6593 ± 0.0006	5.6645 ± 0.0007
$M_{\rm UV}$	-19.97 ± 0.03	-20.63 ± 0.01	-19.26 ± 0.05
$\alpha_{\rm opt}^{R100}$	-1.76 ± 0.1	-1.79 ± 0.07	-1.48 ± 0.11
$\beta_{\rm UV}^{R100}$	-1.69 ± 0.02	-1.96 ± 0.01	-0.88 ± 0.04
$\beta_{\rm Ly\alpha}^{R100}$	-1.11 ± 0.07	-1.38 ± 0.04	1.34 ± 0.32
$I_{\rm [O\,II]\lambda\lambda 3726,3729}$	243 ± 22	279 ± 21	130 ± 23
$z_{\rm N}$	5.6436 ± 0.0001	5.6524 ± 0.0001	5.6504 ± 0.0002
$z_{\rm B}$	5.6483 ± 0.0002	5.6537 ± 0.0001	5.6597 ± 0.0001
$v_{\rm N}$	-480 ± 13	-84 ± 13	-174 ± 17
$v_{\rm B}$	-269 ± 17	-25 ± 14	245 ± 13
FWHM$_{\rm Balmer,N}$	136 ± 6	151 ± 13	300 ± 29
FWHM$_{\rm Balmer,B}$	528 ± 17	492 ± 14	347 ± 8
FWHM$_{\rm [O\,III],N}$	129 ± 4	107 ± 13	300 ± 40
FWHM$_{\rm [O\,III],B}$	655 ± 28	510 ± 19	334 ± 10
$\alpha_{\rm opt}^{\rm R2700}$	-2.32 ± 0.23	-1.81 ± 0.15	-1.4 ± 0.18
$I_{\rm H\beta,N}$	42 ± 3	41 ± 5	12 ± 3
$I_{\rm H\beta,B}$	50 ± 4	49 ± 8	88 ± 4
$I_{\rm H\beta}$	92 ± 5	90 ± 9	100 ± 5
$I_{\rm [O\,III]\lambda 4959,N}$	84 ± 2	36 ± 3	12 ± 2
$I_{\rm [O\,III]\lambda 4959,B}$	48 ± 3	67 ± 3	72 ± 2
$I_{\rm [O\,III]\lambda 4959}$	132 ± 3	102 ± 4	84 ± 2
$I_{\rm [O\,III]\lambda 5007,N}$	249 ± 4	106 ± 8	37 ± 5
$I_{\rm [O\,III]\lambda 5007,B}$	143 ± 9	199 ± 10	215 ± 6
$I_{\rm [O\,III]\lambda 5007}$	393 ± 10	305 ± 13	252 ± 7
$I_{\rm [N\,II]\lambda 6548,N}$	3 ± 1	3 ± 1	19 ± 2
$I_{\rm [N\,II]\lambda 6548,B}$	23 ± 2	40 ± 2	68 ± 2
$I_{\rm [N\,II]\lambda 6548}$	25 ± 2	43 ± 2	87 ± 3
$I_{\rm H\alpha,N}$	157 ± 6	111 ± 11	89 ± 8
$I_{\rm H\alpha,B}$	214 ± 9	307 ± 10	461 ± 9
$I_{\rm H\alpha}$	371 ± 11	418 ± 15	550 ± 12
$I_{\rm [N\,II]\lambda 6584,N}$	8 ± 3	10 ± 4	56 ± 6
$I_{\rm [N\,II]\lambda 6584,B}$	67 ± 6	116 ± 6	201 ± 7
$I_{\rm [N\,II]\lambda 6584}$	75 ± 7	126 ± 7	257 ± 9
$I_{\rm [S\,II]\lambda 6716,N}$	< 37	< 33	< 26
$I_{\rm [S\,II]\lambda 6716,B}$	42 ± 6	60 ± 5	37 ± 5
$I_{\rm [S\,II]\lambda 6716}$	42 ± 6	60 ± 5	37 ± 5
$I_{\rm [S\,II]\lambda 6731,N}$	6 ± 3	< 27	< 27
$I_{\rm [S\,II]\lambda 6731,B}$	37 ± 7	56 ± 5	31 ± 6
$I_{\rm [S\,II]\lambda 6731}$	43 ± 8	56 ± 5	31 ± 6

Table 3. Definitions of line flux ratios used in this work.

Ratio	Definition
R3	[O III] λ5007/Hβ
N2	[N II] λ6584/Hα
S2	[S II] $\lambda\lambda$6716,6731/Hα
RS32	[O III] λ5007/Hβ +[S II] $\lambda\lambda$6716,6731/Hα
O3S2	[O III] λ5007/Hβ /[S II] $\lambda\lambda$6716,6731/Hα
O3N2	[O III] λ5007/Hβ /[N II] λ6584/Hα

The observed line ratios may be used to determine the dust-corrected $SFR_{\rm H\alpha}$. We first calculate the $B-V$ colour excess from the Balmer decrement (e.g. Domínguez et al. 2013; Jones et al. 2024a). Combined with an assumed intrinsic value of $F_{\rm H\alpha}/F_{\rm H\beta} = 2.86$ (Osterbrock 1989),[6] we correct the observed $F_{\rm H\alpha}$ for dust obscuration and use the Kennicutt (1998) scaling law to predict the dust-corrected $SFR_{\rm H\alpha}$ (see Table 4). The sum of dust-corrected $SFR_{\rm H\alpha}$ values over all three components ($150 \pm 18\,{\rm M}_\odot\,{\rm yr}^{-1}$) contains contributions from both obscured and unobscured star formation activity, and is in agreement with the obscured SFR of Capak et al. (2015): $SFR_{\rm IR} = 169^{+32}_{-27}\,{\rm M}_\odot\,{\rm yr}^{-1}$.

We note that the Hα-based value presented here only represents emission from the three circular apertures in Fig. 1, while Capak

[6]This ratio was derived assuming Case B recombination, which has recently been called into question for some galaxies (e.g. Scarlata et al. 2024; McClymont et al. 2025). Since our observed Balmer ratios may be explained with dust attenuation (see Table 4), this assumption appears to be valid here.

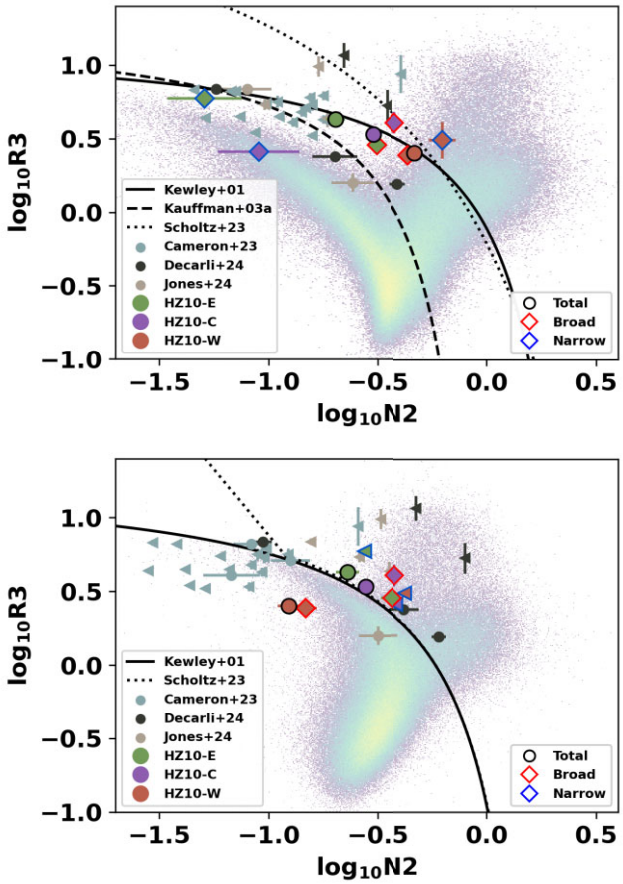

Figure 4. [N II]-BPT (upper) and [S II]-VO87 (lower) plots created using best-fitting line fluxes for each component of HZ10, as derived from the R2700 spectra (see the values in Table 2). Best-fitting narrow components, broad components, and total models for each component are shown with blue, red, and black outlines, respectively. The distributions of low-redshift galaxies from SDSS (MPA-JHU DR8 catalogue; Kauffmann et al. 2003a; Brinchmann et al. 2004) are shown as background points. Left-facing arrows represent 3σ upper limits. We include the demarcation lines for the $z \sim 0$ galaxies of Kewley et al. (2001, solid lines) and Kauffmann et al. (2003b, dashed line), as well as the high-redshift demarcation of Scholtz et al. (2025b, dotted line). We compare our results with values from $z \sim 5.5$–7.0 galaxies observed with the *JWST*/NIRSpec MSA (Cameron et al. 2023) as well as *JWST*/NIRSpec IFU observations of the $z = 6.2342$ quasar system PJ308–21 (Decarli et al. 2024) and the $z = 6.34$–6.36 galaxies in HFLS3 (also known as 1HERMES S350 J170647.8+584623; Riechers et al. 2013, 2022; Jones et al. 2024a).

et al. (2015) integrate over the full field. Integrating over the full field results in a $\mathrm{SFR}_{\mathrm{H}\alpha}$ value that is $< 1\sigma$ discrepant (see Appendix B), suggesting that the star formation in this system is concentrated in the three line-emitting regions.

We may use the [S II] λ6716/[S II] λ6731 ratio of each component to constrain the electron density (Proxauf, Öttl & Kimeswenger 2014). While the resulting uncertainties are large (i.e. up to ∼ 1 dex), the broad contributions of all three components feature similar densities ($\sim 10^3\,\mathrm{cm}^{-3}$). Since no significant narrow [S II] λ6716 emission is detected from any component, we may not constrain the electron density of the source of the narrow emission. The n_e value of the broad emission in each component is comparable to those of other $z \sim 4$–6 galaxies (e.g. Isobe et al. 2023).

Table 4. Properties of HZ10 components derived from line ratio diagnostics. Included are the observed $B - V$ colour excess derived from the Balmer decrement, the dust-corrected SFR derived from Hα intensity, the electron density derived from [S II] λ6716/[S II] λ6731 ratios, and metallicities calculated using the diagnostics of Curti et al. (2020) and the line ratios listed in Table 3. We assume a Salpeter (1955) IMF and Calzetti et al. (2000) extinction law.

	HZ10-E	HZ10-C	HZ10-W
$E(B-V)_{\mathrm{N}}$	0.23 ± 0.07	-0.05 ± 0.13	0.81 ± 0.23
$E(B-V)_{\mathrm{B}}$	0.34 ± 0.08	0.67 ± 0.14	0.52 ± 0.04
$E(B-V)$	0.29 ± 0.05	0.41 ± 0.09	0.56 ± 0.05
$SFR_{\mathrm{H}\alpha,\mathrm{N}}$ ($\mathrm{M}_\odot\,\mathrm{yr}^{-1}$)	9 ± 2	3 ± 1	30 ± 22
$SFR_{\mathrm{H}\alpha,\mathrm{B}}$ ($\mathrm{M}_\odot\,\mathrm{yr}^{-1}$)	17 ± 4	66 ± 29	62 ± 9
$SFR_{\mathrm{H}\alpha}$ ($\mathrm{M}_\odot\,\mathrm{yr}^{-1}$)	25 ± 4	41 ± 12	84 ± 13
$\log_{10}(n_{\mathrm{e,N}}/\mathrm{cm}^{-3})$	–	–	–
$\log_{10}(n_{\mathrm{e,B}}/\mathrm{cm}^{-3})$	3.02 ± 0.95	2.82 ± 0.36	3.25 ± 1.18
$12 + \log_{10}(\mathrm{O/H})_{\mathrm{N}}$	8.32 ± 0.05	8.50 ± 0.05	8.62 ± 0.05
Z_{N} ($Z_\odot$)	0.43 ± 0.07	0.64 ± 0.11	0.85 ± 0.14
$12 + \log_{10}(\mathrm{O/H})_{\mathrm{B}}$	8.51 ± 0.05	8.54 ± 0.05	8.54 ± 0.05
Z_{B} ($Z_\odot$)	0.66 ± 0.11	0.71 ± 0.12	0.70 ± 0.11
$12 + \log_{10}$ (O/H)	8.41 ± 0.05	8.49 ± 0.05	8.54 ± 0.05
Z ($Z_\odot$)	0.52 ± 0.09	0.63 ± 0.10	0.71 ± 0.12

Our dust-corrected line ratios (see Table 3) are combined with the metallicity diagnostics of Curti et al. (2020) to determine the gas-phase metallicity of each component. Note that we only include line fluxes determined from the R2700 data (i.e. excluding [O II] λλ3726,3729), as the complex line shapes and spectral blending cause R100-based line fluxes to be incorrectly estimated. Assuming a solar oxygen abundance of $12 + \log_{10}(\mathrm{O/H}) = 8.69 \pm 0.05$ (Asplund et al. 2009), we find gas-phase metallicities of ∼ 0.53–0.72 solar for the three components (in agreement with Markov et al. 2022). These are higher than most galaxies in this epoch (e.g. Curti et al. 2024), but comparable to the metallicities found in other high-redshift merging systems (e.g. Arribas et al. 2024; Pérez-González et al. 2024; Rodríguez Del Pino et al. 2024; Venturi et al. 2024).

3.3 Spatially resolved analyses

While the component-based analysis allows us to characterize the three primary line-emitting regions and constrain some physical parameters, the nature of the NIRSpec IFU also allows us to explore these properties in a resolved manner. That is, we may extract spectra from each spaxel of the R100 and R2700 cubes and fit each to reveal the ionized gas kinematics, metallicity, and morphology of the complex source HZ10.

3.3.1 R2700 resolved analysis

The R2700 data cube is a rich treasure trove of morpho-kinematic information, but the fact that the spectra of many spaxels exhibit non-symmetric emission lines complicates resolved analysis. These skewed lines could represent tidal interaction features or outflows [we examine evidence for the presence of a broad-line region (BLR) in Section 4.1.1], as well as contamination from emission in other spaxels within the PSF. We explore the R2700 data cube by fitting the spectrum of each spaxel using the flexible line and continuum model detailed in Section 3.2.

The approach of fitting two components to each line (i.e. narrow and broad) is more suitable than a single-Gaussian approach, but may still simplify the distribution and source of flux in the HZ10 field. To

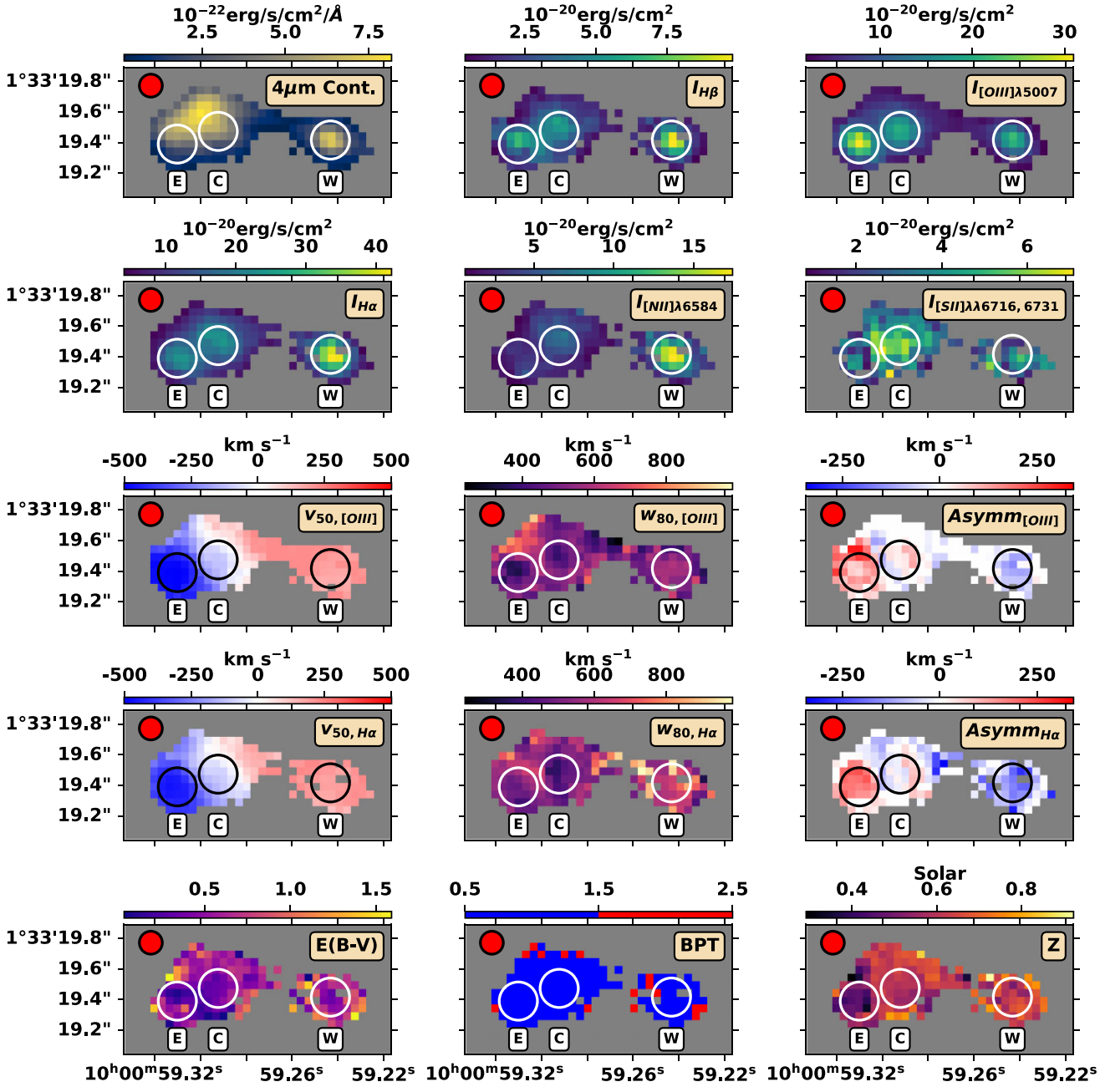

Figure 5. Results of fitting the spectrum of each spaxel in the R2700 data cube. We include the continuum flux at $\lambda_{obs} = 4$ μm, integrated line intensities, and kinematic measures. In addition, we present the colour excess $E(B-V)$, the [N II]-BPT classification of Scholtz et al. (2025b), and the gas-phase metallicity. Hollow circles depict the location of each line peak (see Fig. 1), while the fiducial PSF (FWHM= 0.15″) is depicted by a red circle to the upper left.

test this, we performed a non-parametric kinematic analysis of the spectrally distinct [O III] λ5007 emission (Appendix C). Since the results of the two-Gaussian and non-parametric approaches agree, the two-Gaussian approach is sufficient to capture the asymmetric morpho-kinematics of this field.

Using LMFIT in 'least_squares' mode, we first fit each spectrum with all variables free. The results are inspected, we fix the flux of all line components with S/N< 3 to 0, and re-run the fit until only well-fit lines remain. Once the fit converges, we extract the continuum value, total line flux of each line, and velocity information from each best-fitting model. The results are shown in Fig. 5.

The fits are used to extract relevant kinematic measures for [O III] λ5007 and H α. First, we consider v_X, or the velocity (with respect to a systemic redshift of $z = 5.6543$) at which the cumulative distribution function (CDF) of the best-fitting line model (including both broad and narrow components) reaches a value of Xper cent. This results in estimates of v_{50}, $w_{80} \equiv v_{90} - v_{10}$, and asymmetry= $|v_{50} - v_{90}| - |v_{50} - v_{10}|$ (e.g. Hervella Seoane et al. 2023). These measures respectively represent the line-of-sight velocity, linewidth, and whether the line is skewed to the red or blue.

For each spaxel where H β, [O III] λ5007, [N II] λ6584, and H α are well detected, we apply the [N II]-BPT demarcation line of Scholtz

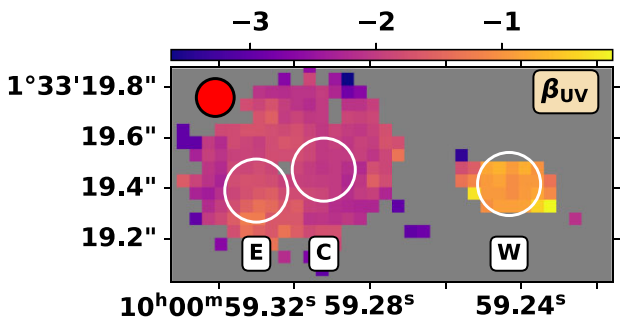

Figure 6. The rest-UV power-law slope (β_{UV}), as derived by fitting the spectrum of each spaxel in the R100 data cube. Hollow circles depict the location of each line peak (see Fig. 1), while the fiducial PSF (FWHM= 0.15 arcsec) is depicted by a red circle to the upper left. The field of view is the same as in Fig. 5.

et al. (2025b) to test for extreme AGN-excitation. $E(B-V)$ is calculated using the observed Balmer decrement for each spaxel when both Hα and Hβ are well determined (i.e. $> 1\sigma$). Dust-corrected line fluxes (see Table 3) are also used to determine the metallicity (Curti et al. 2020).

We find that the continuum emission peaks to the north of the field (Fig. 5). Most of the line flux is concentrated in the three components, with the exception of the weaker [S II] $\lambda\lambda$6716,6731, which is strongest between HZ10-E and HZ10-C. Due to the faintness of [S II] $\lambda\lambda$6716,6731, we are not able to present maps of n_e. The kinematics of [O III] $\lambda\lambda$4959,5007 and the other lines are comparable: a strong east–west velocity gradient with no major trends in w_{80} (expect for a slightly wider linewidth in HZ10-W). HZ10-E and HZ10-W feature red and blue asymmetry, respectively, while HZ10-C straddles a separate gradient of asymmetry.

The distribution of properties is in agreement with the aperture-based analysis of Section 3.2.2 (see Table 4) and the total integrated analysis of Appendix B. As seen in the first two rows of Fig. 5, Hβ, Hα, and [N II] λ6584 are brightest in HZ10-W, while [O III] λ5007 is brightest in HZ10-E. This distribution results in a lower value of R3 for HZ10-W, and thus a higher metallicity (Curti et al. 2020). Most of the spaxels are SF-excited, with the possible exception of a few low-S/N pixels east of HZ10-W. HZ10-W shows the highest $E(B-V)$, followed by HZ10-C and then HZ10-E. HZ10-E shows a low metallicity ($\sim$ 0.3–0.5 solar), while HZ10-C and HZ10-W are higher ($\sim$ 0.5–0.7 solar).

3.3.2 R100 resolved analysis

Next, we may follow the same spectral fitting procedure outlined in Section 3.2 to fit the line and continuum emission in spectra extracted from each spaxel of the R100 data cube. The spectrum of each spaxel is extracted from the R100 cube and is fit using LMFIT in 'leastsq' mode. Because these data feature a broad LSF ($\sim 10^4$ km s^{-1}), they are more suited for characterizing continuum emission than line emission. Thus, we focus on the continuum emission, and only include line emission in our fits in order to reduce their bias on our fits.

The best-fitting continuum power law slopes bluewards of the Balmer break (β_{UV}) are recorded if the corresponding power law normalizations are well determined (i.e. $> 1\sigma$). The resulting map (Fig. 6) reveals that HZ10-W features a very red continuum $\beta_{UV} \sim -1$, while the rest of the field features more standard values of $\beta_{UV} \sim -2$. The values of β_{UV} in each component are further explored in Section 4.3.

4 DISCUSSION

4.1 Lack of evidence for presence of AGN

From the previous Section, it is apparent that HZ10 is a complex system, with a strong velocity gradient and asymmetric emission lines. The emission-line ratio diagnostics are not able to confirm or refute the presence of an AGN, in agreement with the analysis of Saturni et al. (2018). In this other work, the authors compared the location of AGN and SFGs in IRX-β diagrams, finding a low probability for AGN domination in HZ10 (i.e. $\leq$ 30 per cent). Our *JWST*/NIRSpec data allow us to use other methods to search for AGN signatures. Here, we explore whether there is a broad-line region (BLR) in this system (Section 4.1.1), and if there are high-ionization lines detected (Section 4.1.2).

4.1.1 Testing for the presence of a BLR

BLRs, which represent high-dispersion gas in the immediate surroundings of an accreting black hole, have been discovered in multiple $z > 4$ galaxies with *JWST*/NIRSpec through the detection of broad (FWHM$> 10^3$ km s^{-1}) components of permitted lines, typically Balmer hydrogen lines (Hα and Hβ; e.g. Loiacono et al. 2024; Parlanti et al. 2024; Maiolino et al. 2024a; Übler et al. 2024a). Crucially, forbidden lines (including [O III] $\lambda\lambda$4959,5007, [N II] $\lambda\lambda$6548,6584, and [S II] $\lambda\lambda$6716,6731) are not emitted from BLRs due to suppression in high-density environments (e.g. Baskin & Laor 2005; Cresci et al. 2023).

In Section 3.2, we extracted spectra from the R2700 data cube using circular apertures of radius 0.125 arcsec centred on each of the three line peaks, and fit each with a two-component (broad and narrow) model for each line. To allow for the presence of a BLR, we allowed the linewidths of each forbidden line to differ from the linewidths of the Balmer lines. The resulting fits (Fig. 2) and best-fitting values (Table 2) show that the broad component is redshifted in HZ10-E and blueshifted in HZ10-W. Both the Balmer lines and [O III] $\lambda\lambda$4959,5007 feature a broad component with FWHM$< 10^3$ km s^{-1}. Because there is no strong evidence for an extreme broad component (e.g. Parlanti et al. 2024; Übler et al. 2024a), it is likely that the broad component in these spectra does not originate from an extreme BLR, and instead represents a tidal feature or outflow. However, we note that a weak BLR may still be present, contributing to the broad emission.

4.1.2 Lack of high-ionization lines

We also conduct a search for high-ionization lines (ionization energies of $\sim$ 50–100 eV): C IV $\lambda\lambda$1548,1551, He II λ1640, [Ne IV] λ2422,2424, and He II λ4686 (e.g. Feltre et al. 2016; Laporte et al. 2017; Nakajima et al. 2018; Tozzi et al. 2023; Maiolino et al. 2024a). A detection of these lines indicates a hard ionizing spectrum (e.g. Topping et al. 2024b), and they have been used to construct line ratio diagnostics that separate AGN and star-forming environments more successfully than the [N II]-BPT and [S II]-VO87 diagrams (e.g. Shirazi & Brinchmann 2012). On the other hand, some works have used non-detections to argue against photoionization by an AGN (e.g. Williams et al. 2014).

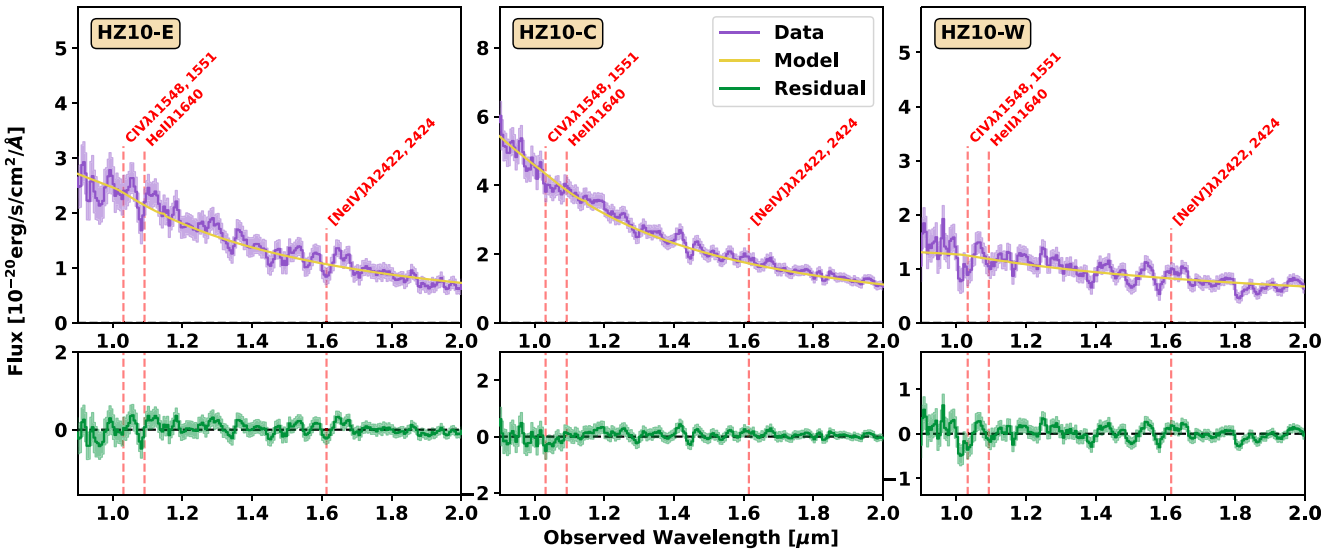

Figure 7. Spectra extracted from the R100 data cube (purple lines), using circular apertures centred on each component, focused on three high-excitation emission lines (red vertical dashed lines). We present a fit to the continuum of each spectrum (yellow line), as well as residuals (green line). The 1σ RMS noise level is shown by the shaded regions.

We search for evidence of these lines in spectra extracted from the R100 data cube using the same component-focused apertures of Section 4.1.1. The resulting spectra around C IVλλ1548,1551, He IIλ1640, and [Ne IV] λ2422,2424 are shown in Fig. 7, where we also present a fit to the continuum. It is clear that none are detected at high significance. Our data show no evidence for significant detections of the rest-optical line He IIλ4686.

These non-detections suggest that the three primary line-emitting components of HZ10 are not dominated by high-ionization regions. However, we note that the spectral range required for the detection of most of these lines is only covered by the low spectral resolution R100 data. Higher spectral resolution observations may reveal fainter and narrower lines (e.g. Bunker et al. 2023; Maiolino et al. 2024a). Through observations of 25 quasars at $z > 6.5$ with *JWST*/NIRCam ('A SPectroscopic survey of biased halos In the Reionization Era'; ASPIRE; Wang et al. 2023), Yang et al. (2023) only found evidence for significant He IIλ4686 emission from one source, suggesting that the non-detection of this line does not exclude the possibility of AGN activity.

4.2 Comparison with ALMA [C II] Data

The *JWST* data presented in this work allow us to characterize the UV- and optical-bright emission of HZ10, but we are still plagued by the effects of dust extinction. This may be examined through the Balmer decrement and colour excess $E(B-V)$ (see Figs 5 and 6), but it is still possible that there are highly attenuated areas whose faint UV emission falls beneath our sensitivity limit. To study areas possibly affected by strong dust obscuration, we leverage high-spatial resolution ALMA data targeting [C II] emission in this field from the CRISTAL survey (Herrera-Camus et al. 2025), which are analysed in a parallel work (Telikova et al. 2024).

Many works have shown that [C II] is a suitable tracer of the total SFR of galaxies in the local and $z > 4$ Universe (e.g. De Looze et al. 2014; Schaerer et al. 2020). However, recent works have argued that it is better suited as a tracer of the atomic (e.g. Vizgan et al. 2022b) or molecular gas (e.g. Zanella et al. 2018; Dessauges-Zavadsky et al. 2020; Vizgan et al. 2022a; D'Eugenio et al. 2023; Aravena et al. 2024), and observations of low metallicity ($Z \sim 0.2$–0.7 solar) dwarf galaxies suggest that [C II] may be a better tracer of total molecular gas content than the commonly used CO or [CI] tracers (Madden et al. 2020). This complexity arises partly from the low ionization potential of carbon (11.26 eV), which enables [C II] emission from multiple phases of the ISM (i.e. warm and dense molecular gas, warm or cold neutral gas; e.g. Langer et al. 2010; Pineda et al. 2013; Gurman et al. 2024). In this work, we interpret [C II] as a tracer of potential and/or ongoing star formation that is less affected by dust obscuration than rest-UV or rest-optical tracers.

We compare the ALMA [C II] distribution with the observed Hα and $\lambda_{obs} = 4$ μm continuum maps derived through spaxel-by-spaxel fits to the R2700 cube (see Section 3.3.1) in Fig. 8. The astrometry of both data sets have been aligned to the *Gaia* DR3 system, so no further spatial shifts are required. The restoring beam of the ALMA data (FWHM of 0.343 arcsec × 0.271 arcsec at a position angle of 54.6°) is large relative to the NIRSpec IFU PSF (FWHM$\sim$ 0.1–0.2 arcsec, D'Eugenio et al. 2024; we assume a fiducial FWHM$=$ 0.15 arcsec), so a direct comparison is slightly ambiguous (the top row of Fig. 8). To better compare these data, we convolve the NIRSpec data set with a custom Gaussian kernel to match the ALMA PSF (photutils function create_matching_kernel; Bradley et al. 2025), as shown in the bottom row of Fig. 8.

By design, the Hα emission (tracing unobscured star formation) is focused in the three line-emitting regions. When convolved to match the ALMA beam to compare to the [C II] morphology, we find a slight east-west offset between the two tracers for HZ10-W and a good match for HZ10-C (as found by Telikova et al. 2024). The [C II] emission does not feature an extension towards HZ10-E (as seen in Hα), suggesting the lack of a strong [C II] peak in HZ10-E. While the $\lambda_{rest} = 4$ μm emission shows a similar morphology as the Hα emission for HZ10-W (i.e. an east–west offset with respect to the [C II] emission), we find that the $\lambda_{rest} = 4$ μm emission is offset to the north-east from HZ10-C.

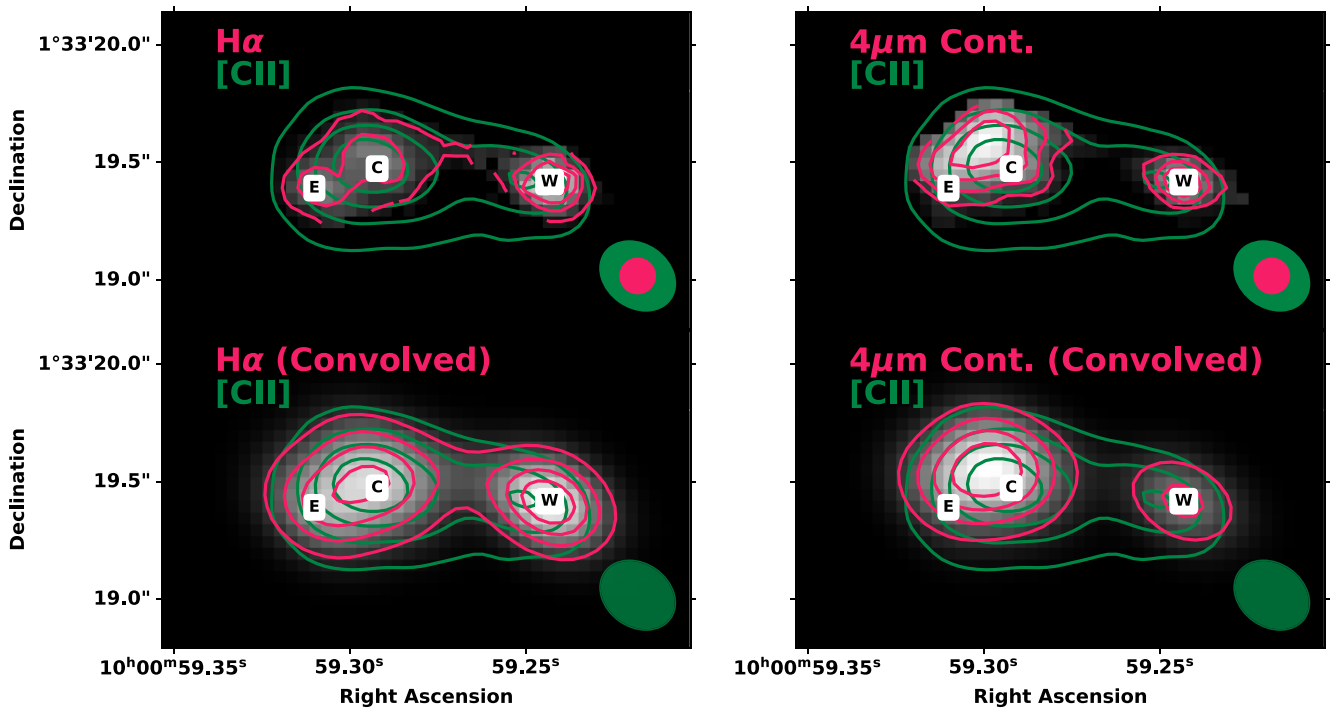

Figure 8. Comparison of Hα (pink contours and grey-scale in left column) and $\lambda_{obs} = 4$ μm emission (pink contours and grey-scale in right column) from our *JWST*/NIRSpec R2700 data cube (Section 3.3.1) with ALMA [C II] emission (green contours in each panel; Telikova et al. 2024). Contours are shown at [20, 40, 60, 80] per cent of the maximum value of each map. The top row shows the NIRSpec data at their native resolution, while NIRSpec data in the lower row are convolved to the same resolution as the ALMA data. The approximate PSFs are shown by filled ellipses.

Offsets between [C II] and UV emission are commonly observed at high redshift (e.g. Maiolino et al. 2015; Inoue et al. 2016; Carniani et al. 2017, 2018; Killi et al. 2024). It has been suggested that these offsets may be caused by a non-isotropic dust distribution, as [C II] may be observed from dusty regions of the cold neutral medium (e.g. Katz et al. 2017). Indeed, Telikova et al. (2024) find that the $\lambda_{rest} \sim 158$ μm FIR continuum emission shows a very similar morphology to the [C II] emission, with the exception of a possible 'bridge' between HZ10-C and HZ10-W (as found in Villanueva et al. 2024). Since this dust would strongly attenuate Hα, it is possible that the east-west offset between [C II] and Hα that we see in HZ10-W represents areas of obscured and unobscured star formation (as supported by the red $\beta_{UV} > -1$ of HZ10-W, see Table 4). The offset of the $\lambda_{rest} = 4$ μm emission from HZ10-C may indicate a region of low ongoing star formation but high stellar mass.

4.3 Nature of components

In this work, we have used the R100 and R2700 data cubes to characterize the HZ10 system in both a component-based and spatially resolved manner. The line emission is concentrated in three peaks (here called HZ10-E, HZ10-C, and HZ10-W), while the continuum emission overlaps these peaks and features additional emission to the north of HZ10-C. All three components show broad [O III] λλ4959,5007 and Balmer lines, which imply tidal features or outflows rather than the presence of a BLR. We cannot confirm the presence of an AGN in each component, as common high-ionization lines are not detected. Here, we synthesize our analyses to propose the natures of different parts of this field.

4.3.1 HZ10-W

Because HZ10-W is spatially separated from the other emission, features overlapping line and continuum emission, and has a nearly uniform w_{80}, [O III] λ5007 rest-frame equivalent width (see Appendix C), and metallicity, we conclude that this is an independent galaxy with a coincident stellar and gas component. Its small spatial separation (< 5 kpc, projected) and line of sight velocity offset (< 500 km s^{-1}) suggest that it is kinematically associated with the rest of HZ10. It features a continuous velocity gradient with HZ10-C, which was previously interpreted as evidence for a single rotating system (e.g. Jones et al. 2017). However, such velocity gradients are often observed in merging systems, where they could represent tidal interactions (e.g. Smit et al. 2018; Hashimoto et al. 2019; Bakx et al. 2020; Scholtz et al. 2025a). There is little to no velocity gradient across the area of HZ10-W, but it features a higher velocity dispersion compared to HZ10-E and HZ10-C (as explored through w_{80}) and strong blue asymmetry in all lines. This combination could imply past tidal interactions or an outflow.

It is clear that HZ10-W has a red continuum ($\beta_{UV} \gtrsim -1$). An in-depth analysis of *JWST*/NIRCam data from the *JWST* Advanced Deep Extragalactic Survey (JADES) revealed that the median UV spectral slope for galaxies at $z \sim 5.9$ is $\beta_{UV} = -2.26 \pm 0.03$ (Topping et al. 2024a). While values around -2 are commonly observed (e.g. Dunlop et al. 2013; Bouwens et al. 2014), there have been cases of very red objects at high redshift (e.g. $\beta_{UV} \sim -1.2$ at $z \sim 7$ in Smit et al. 2018; $\beta_{UV} \sim -1.1$ at $z \sim 6.5$, Matthee et al. 2019). At a given redshift, β_{UV} has been found to correlate with M_*, and anticorrelate with M_{UV} (e.g. Bhatawdekar & Conselice 2021). However, the intrinsic and observed UV slopes may differ due to dust

attenuation (e.g. Wilkins et al. 2013), so redder slopes may indicate larger amounts of dust. This is supported by the east-west offset observed between the FIR continuum and H α, which may indicate an obscuring dust reservoir. Regardless, HZ10-W features the reddest continuum slope, highest metallicity, and highest $E(B-V)$ of the three HZ10 line-emitting components (Table 4), implying a more enriched system than the rest of HZ10.

4.3.2 *HZ10-E and HZ10-C*

HZ10-E and HZ10-C are more complex, as they feature a velocity gradient, independent areas of low w_{80}, and separate peaks of line emission. If they represented a single regular rotating disc, then we would expect to see coincident peaks of line and continuum emission in the centre of a symmetric velocity gradient. Since the peaks are offset from the centre, this could instead represents a pair of galaxies. We note that two distinct peaks could also arise in a disc with a more dust-obscured kinematic centre. While we find little evidence of high obscuration in the spatial region between the two emission peaks, this is still a possibility. HZ10-E also exhibits a redder $\beta_{\rm UV}$, higher $E(B-V)$, and lower metallicity than HZ10-C, arguing in favour of two distinct galaxies.

From comparison between the line and continuum emission (Fig. 1), it is possible that there may be additional galaxies near HZ10-E and HZ10-C. The region to the north-east of these line peaks is UV-luminous but faint in line emission, suggesting a gas-poor population of stars that may be seen immediately post-starburst ($\sim$ 10 Myr). Further evidence for this is given by a comparison of the *JWST* data to new ALMA [C II] data, which shows that this north-east region is not [C II]-luminous. It is true that this region does not show drastic signs of difference in the gas-phase diagnostics (e.g. $\beta_{\rm UV}$, Z, $E(B-V)$), but this may signify that these diagnostics are dominated by gas stripped from HZ10-E and HZ10-C. This also argues against the idea that the north-east emission represents a low-redshift interloper.

4.3.3 *Summary*

Together, these findings suggest that the eastern emission in HZ10 is composed of at least three primary constituents: two star-forming galaxies featuring broad components redshifted with respect to their narrow emission (HZ10-E and HZ10-C) and a gas-poor stellar component to the north. The western emission (HZ10-W) features a blueshifted broad component (with respect to its narrow emission) and coincident UV and line emission. Due to the proximity of these sources, this complex picture may suggest an ongoing merger of multiple galaxies.

In order to classify 'close' pairs of galaxies, it is common to apply the criteria of $\Delta r \lesssim 20$ kpc and $\Delta v \lesssim 500$ km s^{-1} (e.g. Duncan et al. 2019; Ventou et al. 2019; Romano et al. 2021). All of the components in HZ10 meet the spatial separation criterion (<5 projected kpc), and the neighbouring components (i.e. HZ10-E/HZ10-C and HZ10-C/HZ10-W) meet the line-of-sight velocity criterion. Thus, it is likely that all three line-emitting galaxies will merge.

Simulations have shown that major mergers may result in multiple clumps of gas within $\sim$ 5 kpc (e.g. Kohandel et al. 2019; Rizzo et al. 2022), while observations at cosmic noon ($z \sim 2$) have revealed that close mergers may feature nearly continuous velocity gradients (e.g. Simons et al. 2019), as is the case here. The presence of such gas-rich and gas-poor components in the same system is odd at first glance, but similar systems have already been discovered at high redshift (e.g. Jekyll and Hyde; Schreiber et al. 2018; Pérez-González et al. 2024).

As discussed in Telikova et al. (2024), this interpretation is just one possibility (see their fig. 8). The eastern emission (containing HZ10-E and HZ10-C) may represent a single disturbed disc, a merger of two galaxies, or a merger of three galaxies. The single-galaxy possibility is supported by the regular velocity field, but the asymmetry pattern and morphology of line and continuum emission imply complex kinematics and significant variations in ISM conditions. If this is instead a two-galaxy merger, then the line peaks would represent each galaxy, and the asymmetry pattern could be caused by tidal interactions. Finally, HZ10-C may be composed of two galaxies undergoing a very close-scale merger. This system shows a similar morphology to the $z = 4.56$ system DC818760, which was originally detected as a triple merger (Jones et al. 2020), but was resolved into at least four galaxies through higher-resolution observations (Devereaux et al. 2024). In order to determine the true nature of HZ10-E and HZ10-C, additional high-resolution observations are required (e.g. *JWST*/NIRCam).

4.4 Comparison to HZ6 & AzTEC-3

Based on photometric data, Pavesi et al. (2018) find that HZ10 and the starburst galaxy CRLE lie within a galaxy overdensity at $z \sim 5.7$. This situation is quite similar to that of the starburst galaxy AzTEC-3 and star-forming galaxy HZ6[7] at $z = 5.3$ (Capak et al. 2011; Riechers et al. 2014). Both systems feature a starbursting galaxy (SFR $\sim 10^3$ M$_\odot$ yr^{-1}) with a more representative, star-forming galaxy within a projected distance of 100 kpc and a comparable overdensity within a radius of 2 cMpc.

Furthermore, the morpho-kinematics of HZ6 and HZ10 both indicate complex merger behaviour on kpc-scales. A detailed analysis of high-resolution [C II] data from the CRISTAL survey and archival HST/WFC3 F160W images (Ikeda et al. 2025) reveals that the [C II] morphology of HZ6 is well-described by a single 2D Gaussian model, while the rest-UV emission is resolved in three clumps. This is the only CRISTAL source that shows a broad wing in the [C II] spectrum (which may indicate merging or outflow activity; Davies et al. in preparation), which was already seen in lower-resolution data from ALPINE (Béthermin et al. 2020). While results of *JWST*/NIRSpec IFU observations of HZ6 (PID 3045, PI: A. Faisst) are not yet available, the picture from current data is that HZ6 represents a close-separation merger of at least three galaxies (Pavesi et al. 2019; Faisst et al. 2020; Ikeda et al. 2025). With the current *JWST* and ALMA data, it is clear that HZ10 is a merger of at least two galaxies (see Section 4.3 and discussion of Telikova et al. 2024).

While wide-field observations around FIR-bright galaxies have resulted in the detection of galaxy overdensities (e.g. Bischetti et al. 2018; Pavesi et al. 2018; Ginolfi et al. 2022; Calvi, Castignani & Dannerbauer 2023; Zewdie et al. 2025), more detailed analyses of the galaxies that are not the brightest members are needed. Our current data allow us to characterize the morpho-kinematics and ISM conditions of such galaxies on kpc-scales. HZ10 and HZ6 are both complex systems, with multiple closely associated components (<5 projected kpc). Our analysis of HZ10 shows that one component (HZ10-W) is more enriched than the others, possibly indicating a different star formation history. Additional focused observations

[7]HZ6 is also named LBG-1 (e.g. Riechers et al. 2014), DEIMOS_COSMOS_848185 (e.g. Le Fèvre et al. 2020), and CRISTAL-02 (e.g. Ikeda et al. 2025).

of non-dominant galaxies in high-redshift overdensities will enable characterization of their current properties, placing constraints on their histories and informing cosmological models and simulations (e.g. Hashimoto et al. 2023b; Rennehan 2024).

5 CONCLUSIONS

In this work, we present both high ($R \sim 2700$) and low spectral resolution ($R \sim 100$) *JWST*/NIRSpec IFU data of the $z \sim 5.7$ dusty star-forming galaxy HZ10, as part of the GTO programme GA-NIFS. The high spatial resolution (PSF$\sim 0.15''$) of our data opens a new window into the stellar and ionized gas properties of this source, revealing multiple components within a $\sim 1.5''$ diameter region: three components detected in emission lines (HZ10-E, HZ10-C, and HZ10-W) and an additional offset rest-optical continuum source.

We extract spectra from the R2700 data cube using circular apertures centred on each line-emitting component and fit each with a combined continuum and line model (Hβ, [O III] $\lambda\lambda$4959,5007, [N II] $\lambda\lambda$6548,6584, Hα, [S II] $\lambda\lambda$6716,6731). Each line is well fit by a two-component model, suggesting the presence of tidal features. Through line ratio analyses, we find little evidence for AGN domination ([N II]-BPT and [S II]-VO87 diagrams), a high metallicity (0.5–0.7 solar, using the strong line diagnostics of Curti et al. 2020), and electron densities of the broad emission comparable to other galaxies at $z \sim 4$–6: $\log_{10}(n_e/\mathrm{cm}^{-3}) \sim 3$. The R100 spectrum (which features a wider wavelength range) also exhibits emission from the unresolved doublet [O II] $\lambda\lambda$3726,3729, a range of UV spectral slopes ($\beta_{\mathrm{UV}} \sim -2.0$ to -1.0), and no significant Lyα emission (with an upper limit in agreement with a previous detection, see Appendix B).

The great potential of the IFU data is exploited by then exploring each cube on a spaxel-by-spaxel basis. Line emission is focused in the three primary components, while continuum emission ($\lambda_{\mathrm{obs}} = 4\,\mu$m, or $\lambda_{\mathrm{rest}} \sim 0.60\,\mu$m) features an extension to the north. A significant east-west velocity gradient is detected. HZ10-E and HZ10-C show red line asymmetries, while HZ10-W features blue asymmetry. No major trends in metallicity or $E(B-V)$ are detected, while HZ10-W is found to exhibit a red spectral slope $\beta_{\mathrm{UV}} \sim -1$.

We find that since all of the lines (i.e. both Balmer and forbidden lines) features both a narrow and broad component with FWHM $< 10^3\,\mathrm{km\,s^{-1}}$, there is no evidence for a strong BLR. In the same regions, we do not significantly detect high-ionization lines that would indicate AGN photoionization. Thus, the asymmetric line profiles in the current data may indicate the presence of outflows, tidal tails, and/or minor satellites. Further observations at higher spectral resolution are required to confirm this.

Through a comparison to new high-resolution ALMA [C II] data (Telikova et al. 2024), we find that the Hα and [C II] emission are nearly spatially aligned, indicating ongoing star formation from molecular gas reservoirs. Some offsets are detected, indicating dust reservoirs that are obscuring rest-optical and rest-UV emission. On the other hand, the rest UV-optical continuum emission to the north of HZ10-C is offset from the [C II], suggesting a gas-poor population.

Together, our analyses suggest a re-interpretation of the well-studied source HZ10. While previous observations at low spatial resolution suggested a galaxy with a strong rotation gradient and offsets between some tracers, we are now able to resolve multiple separate galaxies. Due to their close spatial and spectral association, they likely represent a merging group. One galaxy is spatially separated, features nearly coincident rest-optical continuum, [C II], and line emission (HZ10-W), and has a blue line asymmetry. To the east of this object lies a complex group of two line emitting peaks (HZ10-E and HZ10-C) with a strong velocity gradient and red line asymmetry. Furthermore, there is a UV-bright population of gas-poor stars to the north of these galaxies which may represent a separate galaxy or a distinct region of HZ10-C. The current data are not yet sufficient to state whether the emission east of HZ10-W represents a single disturbed disc or a multiple merger.

The analysis presented here represents a major step forward in the characterization of the ionized gas morpho-kinematics, ISM conditions, and general nature of a FIR-bright, high-redshift group of galaxies. There are still some ambiguities (e.g. the distribution of Lyα emission, the presence of narrow-line AGNs), which may be remedied by higher spectral resolution NIRSpec/IFU observations in different gratings (e.g. G140H). Future SED analysis of the R100 data presented in this work will result in new estimates on stellar mass and star formation history. Work is already underway on ALMA high-resolution [C II] (Telikova et al. 2024) and FIR-emitting dust analyses (Villanueva et al. 2024). When complete, this field will act as a key prototypical close-separation merger at high-redshift for studies of galaxy evolution.

ACKNOWLEDGEMENTS

We thank the anonymous referee for constructive feedback that enhanced this work. GCJ and AJB acknowledge funding from the 'FirstGalaxies' Advanced Grant from the European Research Council (ERC) under the European Union's Horizon 2020 research and innovation programme (Grant agreement no. 789056). GCJ, FDE and RM acknowledge support by the Science and Technology Facilities Council (STFC), by the ERC through Advanced Grant 695671 'QUENCH', and by the UKRI Frontier Research grant RISEandFALL. KT was supported by ALMA-ANID grant number 31220026. KT, MA, and RHC acknowledge support from the ANID BASAL project FB210003. SA, MP, and BRdP acknowledge grant PID2021-127718NB-I00 funded by the Spanish Ministry of Science and Innovation/State Agency of Research (MICIN/AEI/10.13039/501100011033). SCa acknowledges support from the European Union (ERC, WINGS,101040227). HÜ acknowledges funding by the European Union (ERC APEX, 101164796). Views and opinions expressed are however those of the authors only and do not necessarily reflect those of the European Union or the European Research Council Executive Agency. Neither the European Union nor the granting authority can be held responsible for them. GC acknowledges the support of the INAF Large Grant 2022 'The metal circle: a new sharp view of the baryon cycle up to Cosmic Dawn with the latest generation IFU facilities'. RHC thanks the Max Planck Society for support under the Partner Group project 'The Baryon Cycle in Galaxies' between the Max Planck for Extraterrestrial Physics and the Universidad de Concepción. IL acknowledges support from PID2022-140483NB-C22 funded by AEI 10.13039/501100011033 and BDC 20221289 funded by MCIN by the Recovery, Transformation and Resilience Plan from the Spanish State, by NextGenerationEU from the European Union through the Recovery and Resilience Facility, and from PRIN-MUR project 'PROMETEUS' financed by the European Union–Next Generation EU, Mission 4 Component 1 CUP B53D23004750006. PGP-G acknowledges support from grant PID2022-139567NB-I00 funded by Spanish Ministerio de Ciencia e Innovación MCIN/AEI/10.13039/501100011033, FEDER *Una manera de hacer Europa*. VV acknowledges support from the ALMA-ANID Postdoctoral Fellowship under the award ASTRO21-0062. GCJ would like to thank Elena Bertola, Cosimo Marconcini, and Aayush Saxena for useful discussion and feedback

on the manuscript. This paper makes use of the ALMA data: ADS/JAO. ALMA#2019.1.01075.S. ALMA is a partnership of the ESO (representing its member states), NSF (USA) and NINS (Japan), together with NRC (Canada), MOST and ASIAA (Taiwan), and KASI (Republic of Korea), in cooperation with the Republic of Chile. The Joint ALMA Observatory is operated by the ESO, AUI/NRAO, and NAOJ.

DATA AVAILABILITY

The NIRSpec data used in this work was been obtained within the NIRSpec-IFU GTO programme GA-NIFS (PID 1217) and is publicly available. Data presented in this work will be shared upon reasonable request to the corresponding author.

REFERENCES

Allen M. G., Groves B. A., Dopita M. A., Sutherland R. S., Kewley L. J., 2008, ApJS, 178, 20
Aravena M. et al., 2024, A&A, 682, A24
Arribas S. et al., 2024, A&A, 688, A146
Asplund M., Grevesse N., Sauval A. J., Scott P., 2009, ARA&A, 47, 481
Bakx T. J. L. C. et al., 2020, MNRAS, 493, 4294
Baldwin J. A., Phillips M. M., Terlevich R., 1981, PASP, 93, 5
Baskin A., Laor A., 2005, MNRAS, 358, 1043
Béthermin M. et al., 2020, A&A, 643, A2
Bhatawdekar R., Conselice C. J., 2021, ApJ, 909, 144
Bischetti M. et al., 2018, A&A, 617, A82
Böker T. et al., 2022, A&A, 661, A82
Bouwens R. J. et al., 2014, ApJ, 793, 115
Bradley L. et al., 2025, astropy/photutils: 2.1.0. Zenodo
Brinchmann J., Charlot S., White S. D. M., Tremonti C., Kauffmann G., Heckman T., Brinkmann J., 2004, MNRAS, 351, 1151
Bunker A. J. et al., 2023, A&A, 677, A88
Bunker A. J. et al., 2024, A&A, 690, A288
Calvi R., Castignani G., Dannerbauer H., 2023, A&A, 678, A15
Calzetti D., Armus L., Bohlin R. C., Kinney A. L., Koornneef J., Storchi-Bergmann T., 2000, ApJ, 533, 682
Cameron A. J. et al., 2023, A&A, 677, A115
Cameron A. J., Katz H., Witten C., Saxena A., Laporte N., Bunker A. J., 2024, MNRAS, 534, 523
Capak P. L. et al., 2011, Nature, 470, 233
Capak P. L. et al., 2015, Nature, 522, 455
Carilli C. L., Riechers D., Walter F., Maiolino R., Wagg J., Lentati L., McMahon R., Wolfe A., 2013, ApJ, 763, 120
Carniani S. et al., 2017, A&A, 605, A42
Carniani S. et al., 2018, MNRAS, 478, 1170
Cresci G. et al., 2023, A&A, 672, A128
Curti M., Mannucci F., Cresci G., Maiolino R., 2020, MNRAS, 491, 944
Curti M. et al., 2024, A&A, 684, A75
D'Eugenio C., Daddi E., Liu D., Gobat R., 2023, A&A, 678, L9
D'Eugenio F. et al., 2024, Nat. Astron., 8, 1443
D'Eugenio F. et al., 2025, ApJS, 277, 4
De Looze I. et al., 2014, A&A, 568, A62
Decarli R. et al., 2024, A&A, 689, A219
de Graaff A. et al., 2024, A&A, 684, A87
Delgado-Serrano R., Hammer F., Yang Y. B., Puech M., Flores H., Rodrigues M., 2010, A&A, 509, A78
Della Bruna L. et al., 2020, A&A, 635, A134
Dessauges-Zavadsky M. et al., 2020, A&A, 643, A5
Devereaux T. et al., 2024, A&A, 686, A156
Dimitrijević M. S., Popović L. Č., Kovačević J., Dačić M., Ilić D., 2007, MNRAS, 374, 1181
Dojčinović I., Kovačević-Dojčinović J., Popović L. Č., 2023, Adv. Space Res., 71, 1219
Domínguez A. et al., 2013, ApJ, 763, 145
Dors O. L., Cardaci M. V., Hägele G. F., Ilha G. S., Oliveira C. B., Riffel R. A., Riffel R., Krabbe A. C., 2024, MNRAS, 527, 8193
Duncan K. et al., 2019, ApJ, 876, 110
Dunlop J. S. et al., 2013, MNRAS, 432, 3520
Faisst A. L., Fudamoto Y., Oesch P. A., Scoville N., Riechers D. A., Pavesi R., Capak P., 2020, MNRAS, 498, 4192
Feltre A., Charlot S., Gutkin J., 2016, MNRAS, 456, 3354
Ferreira L., Conselice C. J., Duncan K., Cheng T.-Y., Griffiths A., Whitney A., 2020, ApJ, 895, 115
Fluetsch A. et al., 2021, MNRAS, 505, 5753
Fraternali F., Karim A., Magnelli B., Gómez-Guijarro C., Jiménez-Andrade E. F., Posses A. C., 2021, A&A, 647, A194
Gaia Collaboration, 2016, A&A, 595, A1
Gaia Collaboration, 2021, A&A, 649, A1
Ginolfi M. et al., 2022, Nat. Commun., 13, 4574
Gurman A., Hu C.-Y., Sternberg A., van Dishoeck E. F., 2024, ApJ, 965, 179
Harikane Y. et al., 2020, ApJ, 896, 93
Hashimoto T. et al., 2019, PASJ, 71, 71
Hashimoto T. et al., 2023a, ApJ, 952, 48
Hashimoto T. et al., 2023b, ApJ, 955, L2
Heintz K. E. et al., 2024, Science, 384, 890
Herrera-Camus R. et al., 2022, A&A, 665, L8
Herrera-Camus R. et al., 2025, preprint (arXiv:2505.06340)
Hervella Seoane K., Ramos Almeida C., Acosta-Pulido J. A., Speranza G., Tadhunter C. N., Bessiere P. S., 2023, A&A, 680, A71
Ibar E. et al., 2015, MNRAS, 449, 2498
Ikeda R. et al., 2025, A&A, 693, A237
Inoue A. K. et al., 2016, Science, 352, 1559
Isobe Y., Ouchi M., Nakajima K., Harikane Y., Ono Y., Xu Y., Zhang Y., Umeda H., 2023, ApJ, 956, 139
Jakobsen P. et al., 2022, A&A, 661, A80
Ji X. et al., 2024, MNRAS, 535, 881
Ji X. et al., 2025, preprint (arXiv:2501.13082)
Jones G. C. et al., 2017, ApJ, 850, 180
Jones G. C. et al., 2020, MNRAS, 491, L18
Jones G. C. et al., 2021, MNRAS, 507, 3540
Jones G. C. et al., 2024a, A&A, 682, A122
Jones G. C. et al., 2024b, A&A, 683, A238
Jones G. C. et al., 2025, MNRAS, 536, 2355
Katz H., Kimm T., Sijacki D., Haehnelt M. G., 2017, MNRAS, 468, 4831
Kauffmann G. et al., 2003a, MNRAS, 341, 33
Kauffmann G. et al., 2003b, MNRAS, 346, 1055
Kennicutt R. C., Jr, 1998, ApJ, 498, 541
Kewley L. J., Dopita M. A., Sutherland R. S., Heisler C. A., Trevena J., 2001, ApJ, 556, 121
Killi M. et al., 2024, MNRAS, 531, 3222
Kohandel M., Pallottini A., Ferrara A., Zanella A., Behrens C., Carniani S., Gallerani S., Vallini L., 2019, MNRAS, 487, 3007
Kretschmer M., Dekel A., Teyssier R., 2022, MNRAS, 510, 3266
Kuhn V., Guo Y., Martin A., Bayless J., Gates E., Puleo A., 2024, ApJ, 968, L15
Laigle C. et al., 2016, ApJS, 224, 24
Langer W. D., Velusamy T., Pineda J. L., Goldsmith P. F., Li D., Yorke H. W., 2010, A&A, 521, L17
Laporte N., Nakajima K., Ellis R. S., Zitrin A., Stark D. P., Mainali R., Roberts-Borsani G. W., 2017, ApJ, 851, 40
Le Fèvre O. et al., 2020, A&A, 643, A1
Le Tiran L., Lehnert M. D., van Driel W., Nesvadba N. P. H., Di Matteo P., 2011, A&A, 534, L4
Lelli F., Di Teodoro E. M., Fraternali F., Man A. W. S., Zhang Z.-Y., De Breuck C., Davis T. A., Maiolino R., 2021, Science, 371, 713
Loiacono F. et al., 2024, A&A, 685, A121
Madden S. C. et al., 2020, A&A, 643, A141
Maiolino R. et al., 2015, MNRAS, 452, 54
Maiolino R. et al., 2024a, Nature, 627, 59
Maiolino R. et al., 2024b, A&A, 691, A145
Markov V., Carniani S., Vallini L., Ferrara A., Pallottini A., Maiolino R., Gallerani S., Pentericci L., 2022, A&A, 663, A172

Marshall M. A. et al., 2023, A&A, 678, A191
Matthee J. et al., 2019, ApJ, 881, 124
Mazzilli Ciraulo B., Melchior A.-L., Maschmann D., Katkov I. Y., Halle A., Combes F., Gelfand J. D., Al Yazeedi A., 2021, A&A, 653, A47
McClymont W. et al., 2025, MNRAS, 540, 190
Murayama T. et al., 2007, ApJS, 172, 523
Nakajima K., Maiolino R., 2022, MNRAS, 513, 5134
Nakajima K. et al., 2018, A&A, 612, A94
Napolitano L. et al., 2024, A&A, 688, A106
Neeleman M., Prochaska J. X., Kanekar N., Rafelski M., 2020, Nature, 581, 269
Newville M., Stensitzki T., Allen D. B., Ingargiola A., 2014, LMFIT: Non-Linear Least-Square Minimization and Curve-Fitting for Python. Zenodo. Available at: https://zenodo.org/records/11813
Nguyen N. H., Lira P., Trakhtenbrot B., Netzer H., Cicone C., Maiolino R., Shemmer O., 2020, ApJ, 895, 74
Novak M. et al., 2019, ApJ, 881, 63
Osterbrock D. E., 1989, Astrophysics of Gaseous Nebulae and Active Galactic Nuclei. University Science Books, Mill Valley, CA
Pallottini A., Ferrara A., Gallerani S., Vallini L., Maiolino R., Salvadori S., 2017, MNRAS, 465, 2540
Parlanti E. et al., 2024, A&A, 684, A24
Pavesi R. et al., 2016, ApJ, 832, 151
Pavesi R. et al., 2018, ApJ, 861, 43
Pavesi R., Riechers D. A., Faisst A. L., Stacey G. J., Capak P. L., 2019, ApJ, 882, 168
Pérez-González P. G. et al., 2024, preprint (arXiv:2405.03744)
Perna M. et al., 2020, A&A, 643, A139
Perna M. et al., 2023, A&A, 679, A89
Perna M. et al., 2025, A&A, 696, A59
Pineda J. L., Langer W. D., Velusamy T., Goldsmith P. F., 2013, A&A, 554, A103
Posses A. C. et al., 2023, A&A, 669, A46
Proxauf B., Öttl S., Kimeswenger S., 2014, A&A, 561, A10
Rennehan D., 2024, ApJ, 975, 114
Richings A. J., Faucher-Giguère C.-A., Stern J., 2021, MNRAS, 503, 1568
Riechers D. A. et al., 2013, Nature, 496, 329
Riechers D. A. et al., 2014, ApJ, 796, 84
Riechers D. A., Weiss A., Walter F., Carilli C. L., Cox P., Decarli R., Neri R., 2022, Nature, 602, 58
Rizzo F., Vegetti S., Powell D., Fraternali F., McKean J. P., Stacey H. R., White S. D. M., 2020, Nature, 584, 201
Rizzo F., Kohandel M., Pallottini A., Zanella A., Ferrara A., Vallini L., Toft S., 2022, A&A, 667, A5
Rodrigues M., Hammer F., Flores H., Puech M., Athanassoula E., 2017, MNRAS, 465, 1157
Rodríguez Del Pino B. et al., 2024, A&A, 684, A187
Roman-Oliveira F., Fraternali F., Rizzo F., 2023, MNRAS, 521, 1045
Romano M. et al., 2021, A&A, 653, A111
Salpeter E. E., 1955, ApJ, 121, 161
Saturni F. G., Mancini M., Pezzulli E., Tombesi F., 2018, A&A, 617, A131
Scarlata C., Hayes M., Panagia N., Mehta V., Haardt F., Bagley M., 2024, preprint (arXiv:2404.09015)
Schaerer D. et al., 2020, A&A, 643, A3
Scholtz J. et al., 2025a, MNRAS, 539, 2463
Scholtz J. et al., 2025b, A&A, 697, A175
Schreiber C. et al., 2018, A&A, 611, A22
Scoville N. et al., 2007, ApJS, 172, 1
Servén D., Brummitt C., 2018, pyGAM: Generalized Additive Models in Python. Zenodo
Shirazi M., Brinchmann J., 2012, MNRAS, 421, 1043
Simons R. C. et al., 2019, ApJ, 874, 59
Smit R. et al., 2018, Nature, 553, 178
Sugahara Y. et al., 2021, ApJ, 923, 5
Tacchella S. et al., 2025, MNRAS, 540, 851
Telikova K. et al., 2024, preprint (arXiv:2411.09033)
Topping M. W. et al., 2024a, MNRAS, 529, 3301
Topping M. W. et al., 2024b, MNRAS, 529, 4087
Tozzi G., Maiolino R., Cresci G., Piotrowska J. M., Belfiore F., Curti M., Mannucci F., Marconi A., 2023, MNRAS, 521, 1264
Tsukui T., Iguchi S., 2021, Science, 372, 1201
Übler H. et al., 2023, A&A, 677, A145
Übler H. et al., 2024a, MNRAS, 531, 355
Übler H. et al., 2024b, MNRAS, 533, 4287
Ulivi L. et al., 2025, A&A, 693, A36
Umeda H., Ouchi M., Nakajima K., Harikane Y., Ono Y., Xu Y., Isobe Y., Zhang Y., 2024, ApJ, 971, 124
Vallini L., Ferrara A., Pallottini A., Carniani S., Gallerani S., 2020, MNRAS, 495, L22
Veilleux S., Osterbrock D. E., 1987, ApJS, 63, 295
Ventou E. et al., 2019, A&A, 631, A87
Venturi G. et al., 2024, A&A, 691, A19
Vieira D., Riechers D. A., Pavesi R., Faisst A. L., Schinnerer E., Scoville N. Z., Stacey G. J., 2022, ApJ, 925, 174
Villanueva V. et al., 2024, A&A, 691, A133
Vizgan D. et al., 2022a, ApJ, 929, 92
Vizgan D., Heintz K. E., Greve T. R., Narayanan D., Davé R., Olsen K. P., Popping G., Watson D., 2022b, ApJ, 939, L1
Wang F. et al., 2023, ApJ, 951, L4
Wilkins S. M., Bunker A., Coulton W., Croft R., di Matteo T., Khandai N., Feng Y., 2013, MNRAS, 430, 2885
Williams R. J. et al., 2014, MNRAS, 439, 2096
Witstok J. et al., 2025, Nature, 639, 897
Yang J. et al., 2023, ApJ, 951, L5
Zanella A. et al., 2018, MNRAS, 481, 1976
Zewdie D. et al., 2025, A&A, 694, A121

APPENDIX A: R100/R2700 ASTROMETRY

As mentioned in Section 2, we verified that the R100 data were aligned with the *Gaia* DR3 astrometric frame through comparisons to aligned *HST* images from the MAST archive. These comparisons are shown in the top row of Fig. A1. We also verify that the R100 and R2700 data cubes are aligned to the same frame by collapsing each over wavelength ranges corresponding to Hβ, [O III] $\lambda\lambda$4959,5007, and Hα +[N II] $\lambda\lambda$6548,6584 (see the bottom row of Fig. A1). As seen in Fig. A1, these maps thus do not suffer from any astrometric issues (i.e. rotation, scaling, or systematic offsets).

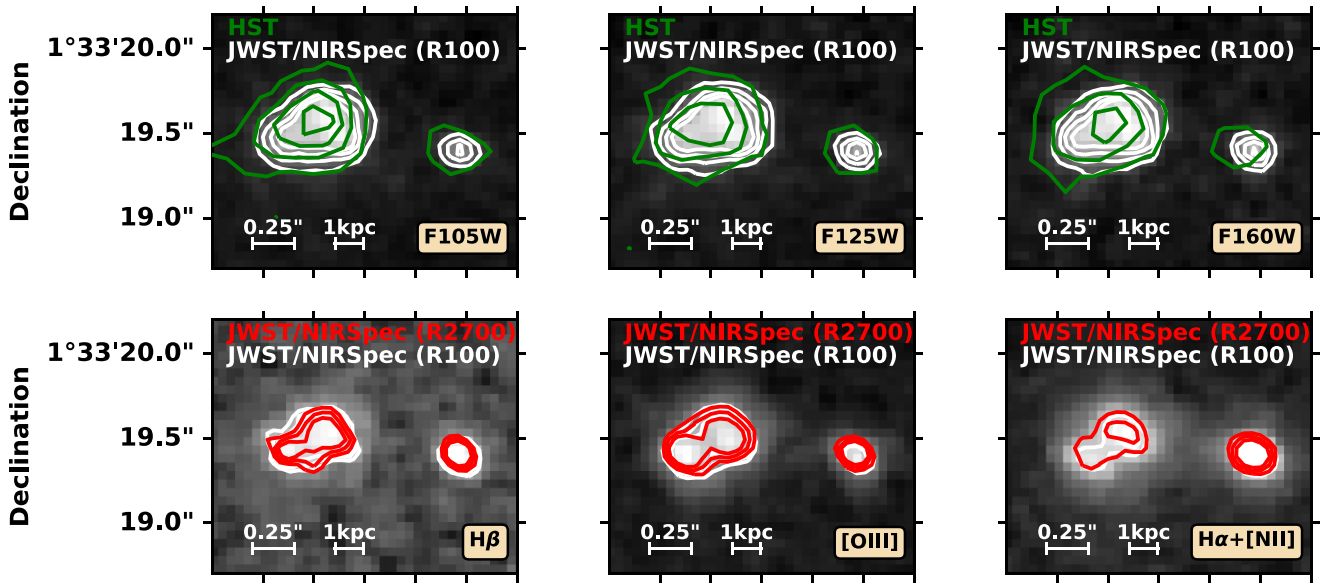

Figure A1. Comparison of astrometric alignment of data using integrated intensity maps of *JWST*/NIRSpec IFU and *HST* data. The top row compares *JWST*/NIRSpec IFU (R100, background grey-scale and white contours) and *HST* images (green contours) over three *HST*/WFC3 filters. The bottom row instead compares the two *JWST*/NIRSpec IFU data cubes (R100, background grey-scale and white contours; R2700, red contours) over the wavelengths corresponding to three emission lines.

APPENDIX B: INTEGRATED SPECTRAL ANALYSIS

In the main body of this work, we characterized the HZ10 field by fitting spectra extracted from the line peaks (Section 3.2) and from each spaxel (Section 3.3). This revealed that HZ10 is not a single homogeneous source, but is composed of several galaxies with different conditions and kinematics. Since an analysis of the full field will average over all of the individual galaxies, we avoided this analysis. But since previous works examined HZ10 as a single system, it is worthwhile to study the integrated R100 spectrum for comparison to the literature. The kinematic complexity of HZ10 (i.e. asymmetric lines) dictates that this approach does not capture the full behaviour of the system. Thus, we only present selected results from this analysis.

We begin by extracting integrated spectra from the R100 data cube using a large elliptical aperture centred on 10m00m59.27s 01°33′19.″40 with major and minor axes of 1.6 and 1.0 arcsec, respectively (see dashed white ellipse in Fig. 1). This aperture was chosen to contain all significant line and detection emission detected

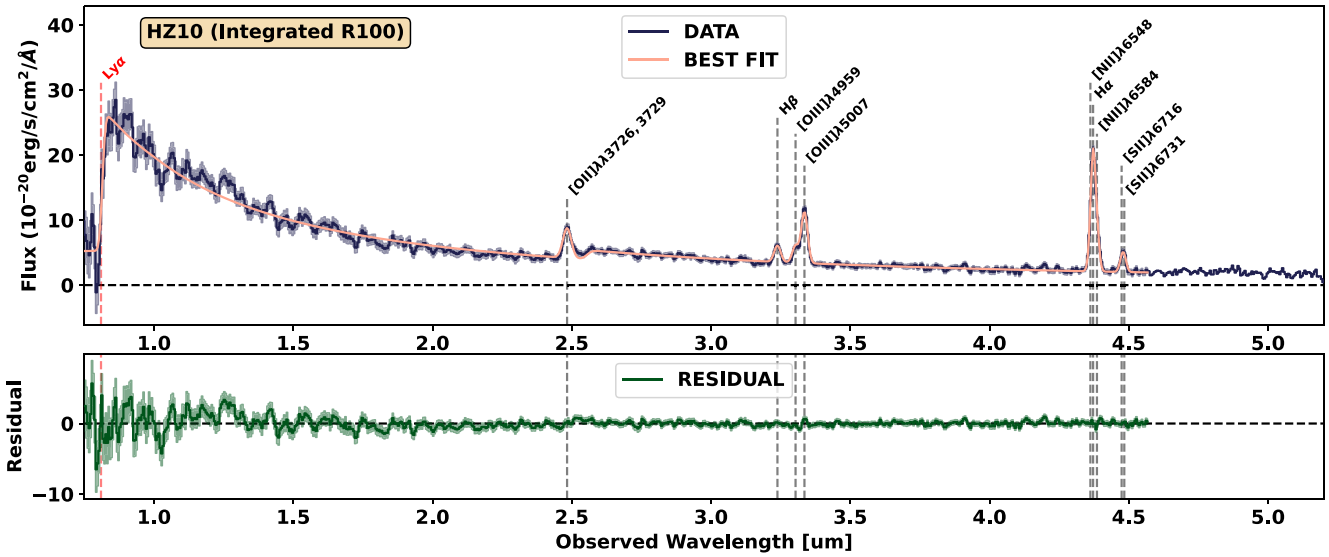

Figure B1. Integrated spectrum extracted from the R100 data cube using the elliptical aperture of Fig. 1. The best-fitting model is shown by the tan line, as well as the residuals (green line). The wavelengths of each line (using the best-fitting $z_{\rm sys}$) are shown by dashed vertical lines. The expected wavelength of Lyα (which is not detected) is marked with a dashed red line. Uncertainties (1σ) for the extracted spectrum and residuals are shown by shaded regions.

by our *JWST*/NIRSpec IFU observations, and is larger than the elliptical aperture used by Telikova et al. (2024) to examine the total [C II] spectrum. The line and continuum emission of the extracted spectrum is fit using a procedure identical to that of Section 3.2, and the resulting fit is shown in Fig. B1.

The continuum is well-detected in the R100 spectrum, resulting in $M_{\rm UV} = -22.22 \pm 0.02$ and $\beta_{\rm UV} = -1.71 \pm 0.02$, in agreement with previous observations (e.g. Capak et al. 2015). The best-fitting Balmer line fluxes result in a colour excess that lies between the values of each component ($E(B-V) = 0.44 \pm 0.22$). Correcting for this dust attenuation results in a large $SFR_{\rm H\alpha} = 380 \pm 200\,{\rm M}_\odot\,{\rm yr}^{-1}$, where the large uncertainty is due to the large uncertainty in $E(B-V)$. This value is in agreement with both the $SFR_{\rm [C\,II]} = 169^{+32}_{-27}\,{\rm M}_\odot\,{\rm yr}^{-1}$ from Capak et al. (2015) and the total $SFR_{\rm H\alpha}$ of the three line-emitting components we study here ($SFR_{\rm H\alpha} = 150 \pm 18\,{\rm M}_\odot\,{\rm yr}^{-1}$). Similarly, the total best-fitting metallicity ($Z = 0.65 \pm 0.05$ solar) is comparable to the metallicities of each line-emitting region (see Table 4).

We do not detect Ly α emission in the R100 integrated spectrum, which yields a 3σ upper limit on the Ly α rest-frame equivalent width of $REW_{\rm Ly\alpha} < 11$ Å. Murayama et al. (2007) detected Ly α with an observed-frame equivalent width of 75 ± 22 Å, which corresponds to a rest-frame value of 11.3 ± 3.3 Å (assuming $z_{\rm [C\,II]}$ from Pavesi et al. 2016). Since this previous work predicted the Ly α flux using a large circular aperture of diameter 3 arcsec, this slightly larger $REW_{\rm Ly\alpha}$ may suggest that HZ10 exhibits a Ly α halo (although an integration over the full IFU field of view does not return a significant Lyα detection). On the other hand, the assumed redshift in the previous work ($z = 5.7$) is slightly larger than the true redshift of this source, and the $REW_{\rm Ly\alpha}$ value is based on fits to photometry. Taking into account the uncertainties, our non-detection of Ly α is not in disagreement with previous results, although follow-up observations at higher spectral resolution (e.g. *JWST*/NIRSpec IFU G140H/F070LP or the Multi Unit Spectroscopic Explorer [MUSE] on the Very Large Telescope [VLT]) are needed to confirm this.

APPENDIX C: [O III]5007 NON-PARAMETRIC KINEMATIC ANALYSIS

Throughout this work, we have modelled each line in the R2700 spectra using two Gaussians (i.e. narrow and broad). However, this simple model may underestimate the complexity of the system. To examine this, we produce non-parametric morpho-kinematic maps for the strong, spectrally distinct line [O III] λ5007 and compare them to maps produced using our two-Gaussian model.

First, we isolate all data within $\pm 1500\,{\rm km\,s}^{-1}$ of the systemic redshift (here assumed to be equal to $z_{\rm [C\,II]} = 5.6543$; Pavesi et al. 2016) and extract spectra for each spaxel. The continuum level for each spectrum is assumed to be constant, and is derived by creating a cumulative distribution function (CDF) of the line-free data (here assumed to be all data in $[-1500, -750]_\cup[750,1500]\,{\rm km\,s}^{-1}$) and fitting this with a first-order polynomial (scipy curve_fit). If the resulting fit features a positive, well-determined slope, it is used

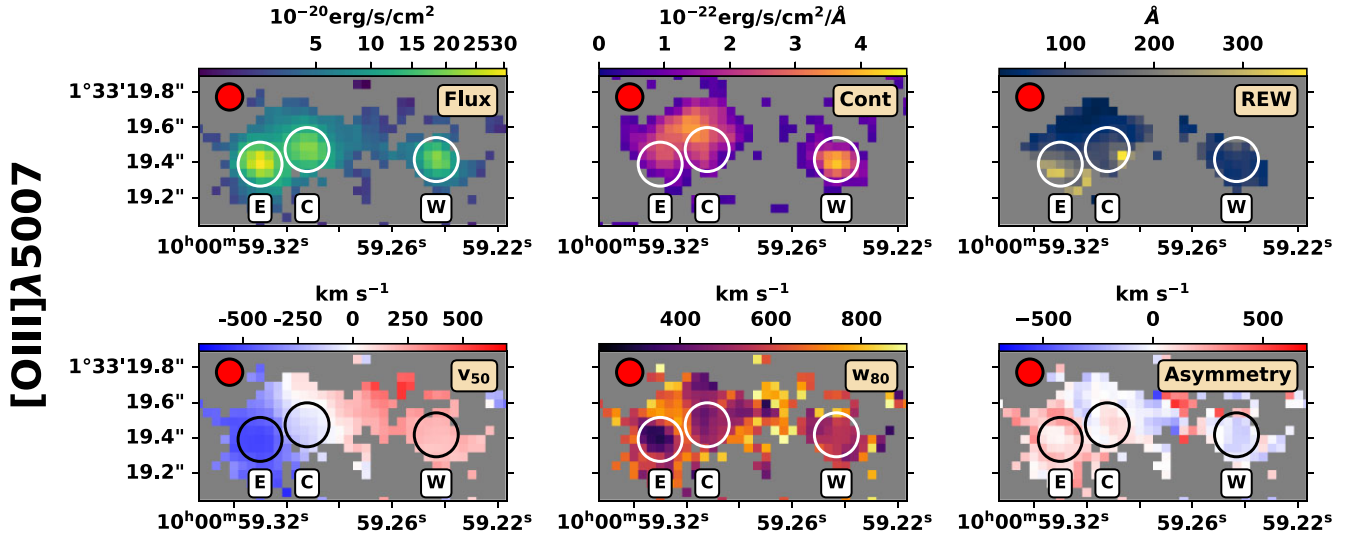

Figure C1. Morpho-kinematic maps of [O III] λ5007. We present the integrated line flux, continuum flux, rest-frame EW, v_{50}, w_{80}, and asymmetry per spaxel. The location of each component is marked with a hollow circle, and the fiducial PSF is represented by a red ellipse to the upper left.

as the continuum flux for the spaxel, which is then subtracted from the spectrum.

The resulting line-only spectra for each spaxel are then used to derive spectral CDFs, which are normalized such that their highest and lowest values are set to unity and zero, respectively. Using PYGAM[8] (Servén & Brummitt 2018), we fit each normalized CDF with a monotonically increasing spline function. If the best fit spans the central 80 per cent of the continuum CDF (i.e. a minimum value less than 0.1 and a maximum value greater than 0.9) and PYGAM reports a good fit (i.e. pseudo-R-squared value greater than 0.9), we record the best-fitting model.

The fits are used to extract the integrated line flux (F_L), continuum flux (S_C), the rest-frame equivalent width, and relevant kinematic measures: v_{50}, w_{80}, and asymmetry$= |v_{50} - v_{90}| - |v_{50} - v_{10}|$ (e.g. Hervella Seoane et al. 2023). We exclude spaxels with unrealistic kinematic measures caused by low signal (i.e. $|v_{50}| > 700\,\mathrm{km\,s^{-1}}$). The line and continuum fluxes are used to derive a rest-frame equivalent width. All acceptable fits are then used to create the morpho-kinematic maps shown in Fig. C1.

The results of this analysis (Fig. C1) are very similar to those of our two-Gaussian approach (Fig. 5). The [O III] λ5007 emission exhibits peaks in three locations, the continuum emission peaks in HZ10-W and to the north of HZ10-E and HZ10-C, a smooth east-west velocity gradient is observed, and the asymmetry pattern is maintained. Since the results of this more detailed kinematic analysis agrees with the two-Gaussian model, we use the two-Gaussian model in this work.

[8]A python package to fit generalized additive models (https://pygam.readthedocs.io/en/latest/.)

[1]*Department of Physics, University of Oxford, Denys Wilkinson Building, Keble Road, Oxford OX1 3RH, UK*
[2]*Kavli Institute for Cosmology, University of Cambridge, Madingley Road, Cambridge CB3 0HA, UK*
[3]*Cavendish Laboratory, University of Cambridge, 19 JJ Thomson Avenue, Cambridge CB3 0HE, UK*
[4]*Instituto de Estudios Astrofísicos, Facultad de Ingeniería y Ciencias, Universidad Diego Portales, Av. Ejército Libertador 441, 8370191 Santiago, Chile*
[5]*Centro de Astrobiología (CAB, CSIC-INTA), Departamento de Astrofísica, Cra. de Ajalvir Km. 4, E-28850 – Torrejón de Ardoz, Madrid, Spain*
[6]*Scuola Normale Superiore, Piazza dei Cavalieri 7, I-56126 Pisa, Italy*
[7]*Sorbonne Université, CNRS, UMR 7095, Institut d'Astrophysique de Paris, 98 bis bd Arago, F-75014 Paris, France*
[8]*Department of Physics and Astronomy, University College London, Gower Street, London WC1E 6BT, UK*
[9]*Max-Planck-Institut für extraterrestrische Physik, Gießenbachstraße 1, D-85748 Garching, Germany*
[10]*NRC Herzberg, 5071 West Saanich Road, Victoria BC V9E 2E7, Canada*
[11]*European Space Agency, c/o STScI, 3700 San Martin Drive, Baltimore, MD 21218, USA*
[12]*INAF – Arcetri Astrophysical Observatory, Largo E. Fermi 5, I-50125, Italy*
[13]*European Southern Observatory, Karl-Schwarzschild-Strasse 2, D-85748 Garching, Germany*
[14]*Instituto de Astrofísica, Facultad de Física, Pontificia Universidad Católica de Chile, Santiago 7820436, Chile*
[15]*Las Campanas Observatory, Carnegie Institution of Washington, Raúl Bitrán 1200, La Serena, Chile*
[16]*Departamento de Astronomía, Universidad de Concepción, Barrio Universitario, Concepción, Chile*
[17]*Dipartimento di Fisica e Astronomia, Università di Firenzeà di Firenze, Via G. Sansone 1, I-50019 Sesto Fiorentino, Firenze, Italy*

This paper has been typeset from a TEX/LATEX file prepared by the author.